

Local Zones of Endoplasmic Reticulum Complexity Confine Cargo in Neuronal Dendrites

Tingting Cui-Wang,^{1,5} Cyril Hanus,^{1,5} Tao Cui,² Thomas Helton,³ Jennifer Bourne,⁴ Deborah Watson,⁴ Kristen M. Harris,⁴ and Michael D. Ehlers^{1,3,*}

¹Department of Neurobiology, Duke University Medical Center, Durham, NC 27710, USA

²Department of Electrical Engineering, California Institute of Technology, Pasadena, CA 91125, USA

³Pfizer Global Research and Development, Neuroscience Research Unit, Groton, CT 06340, USA

⁴Department of Neurobiology, Center for Learning and Memory, the University of Texas at Austin, TX 78705, USA

⁵These authors contributed equally to this work

*Correspondence: michael.ehlers@pfizer.com

DOI 10.1016/j.cell.2011.11.056

SUMMARY

Following synthesis, integral membrane proteins dwell in the endoplasmic reticulum (ER) for variable periods that are typically rate limiting for plasma membrane delivery. In neurons, the ER extends for hundreds of microns as an anastomosing network throughout highly branched dendrites. However, little is known about the mobility, spatial scales, or dynamic regulation of cargo in the dendritic ER. Here, we show that membrane proteins, including AMPA-type glutamate receptors, rapidly diffuse within the continuous network of dendritic ER but are confined by increased ER complexity at dendritic branch points and near dendritic spines. The spatial range of receptor mobility is rapidly restricted by type I mGluR signaling through a mechanism involving protein kinase C (PKC) and the ER protein CLIMP63. Moreover, local zones of ER complexity compartmentalize ER export and correspond to sites of new dendritic branches. Thus, local control of ER complexity spatially scales secretory trafficking within elaborate dendritic arbors.

INTRODUCTION

Most neurons possess highly branched dendrites with thousands of synaptic contacts, a geometry that allows for spatial segregation and integration of diverse signals (Spruston, 2008). The functional properties of dendrites are highly compartmentalized, with individual dendritic segments possessing distinct electrophysiological properties, synaptic inputs, and molecular composition (Losonczy et al., 2008; Matsuzaki et al., 2004). The partitioning of dendrites into functionally distinct segments relies on local regulation of receptor and ion channel distribution in the dendritic membrane (Nicholson et al., 2006). Although regulated transport of membrane components is a requisite for

neuronal morphogenesis, synapse modification, and dendritic plasticity (Kennedy and Ehlers, 2006), the organelles and cellular machinery for spatially restricted dendritic trafficking are poorly understood.

Local dendritic synthesis and secretory processing of membrane cargo, and in particular α -amino-3-hydroxyl-5-methyl-4-isoxazole-propionate (AMPA)-type glutamate receptors provide attractive mechanisms for spatially delimited modification of dendritic segments (Sutton et al., 2006). However, unlike cytoplasmic proteins, which require only mRNA and ribosomes, local production of membrane proteins requires the entire complement of secretory organelles (Hanus and Ehlers, 2008). Yet, little is known about the local dynamics and regulation of AMPA receptors and other dendritic membrane cargo in early secretory compartments.

Recent studies indicate that the entire cast of secretory organelles is present in some dendrites (Gardiol et al., 1999; Horton and Ehlers, 2003). In particular, the endoplasmic reticulum (ER) exists as a continuous anastomosing network in dendrites (Cooney et al., 2002; Spacek and Harris, 1997; Terasaki et al., 1994). For numerous synaptic receptors and notably AMPA receptors (Penn et al., 2008), ER export is rate-limiting for plasma membrane delivery. For slowly exported cargo, diffusion within the ER determines the spatial range of cargo transport to the plasma membrane (Herpers and Rabouille, 2004). Interestingly, AMPA receptors dwell in the ER for variable periods up to several hours (Greger et al., 2002), raising the possibility that dwell time and ER mobility determine the spatial domain over which nascent receptors are delivered to the dendritic plasma membrane. Receptor diffusion at the cell surface has emerged as a critical feature of synaptic physiology (Newpher and Ehlers, 2008). However, the internal diffusion of receptors within the dendritic ER has not been examined, despite a potentially large influence on the spatial scale over which dendritic membrane composition is modified.

Here, we show that newly synthesized membrane proteins, including AMPA receptors, rapidly diffuse within the continuous network of the dendritic ER. Quantitative photobleaching, super-resolution imaging, and ultrastructural analysis reveal that

nascent cargo diffusion is inhomogeneous, with zones of diffusional confinement corresponding to local domains of increased ER complexity near dendritic spines, at dendritic branch points (BPs), and near Golgi outposts (GOs). The spatial range of receptor mobility in the ER becomes progressively limited over neuronal development and is rapidly restricted by group I mGluR signaling through a mechanism involving protein kinase C (PKC) and the microtubule-binding ER protein CLIMP63. Site-specific phosphorylation of CLIMP63 increases ER complexity, thereby trapping nascent membrane proteins within smaller domains of diffusional confinement. Such local zones of ER complexity correspond to domains of ER export and sites of new dendritic branch formation. Correspondingly, manipulations that increase or decrease ER complexity alternately promote or reduce dendritic branching. Finally, increased ER complexity promotes AMPA receptor surface expression and increases synaptic strength. Taken together, these results define a mechanism for compartmentalized trafficking in geometrically complex cells.

RESULTS

Rapid but Spatially Restricted Diffusion of Membrane Proteins in the Dendritic ER

Prior to reaching the plasma membrane, newly synthesized membrane proteins are assembled in the somatodendritic ER where their mobility is unknown. To compare the diffusion of nascent AMPA receptors to that of freely diffusing ER and cell-surface membrane proteins, we engineered various integral membrane GFP fusions and measured fluorescence recovery after photobleaching (FRAP) in hippocampal neurons (Figure 1A and Movie S1 available online). GFP-fusions of ER-retained GluA1 and GluA2 subunits mimicking nascent receptors (ER-GluA1 and ER-GluA2) were generated by introducing point mutations in their glutamate binding sites (Figures 1B and 1C and Figures S1A–S1D). The dynamics of ER-GluA1/2 in dendrites were compared to that of ER-VSVG (Figures 1D and 1E and Figures S1E–S1H and S2), an ER-retained version of the vesicular stomatitis virus glycoprotein (VSVG) that freely diffuses in the ER membrane, to the ER calcium-pump SERCA2a whose dynamics have been characterized (Fukatsu et al., 2004), and to two freely moving plasma membrane proteins, PM-phluo and GT-46 (Figures S1I and S1J).

As expected, ER-GluA1/2 and ER-VSVG were diffusely distributed throughout the dendritic volume (Figure 1C and Figures S1B, S1F, and S1M), consistent with an ER distribution (Cooney et al., 2002; Gardiol et al., 1999; Spacek and Harris, 1997). FRAP showed that GluA2, VSVG and SERCA2a had similar mobility in the dendritic ER, while GluA1 had slightly slower recovery kinetics (Figure 1E, top panel). Determination of apparent diffusion coefficients using a three-dimensional diffusion model (Figure S1K) confirmed the rapid motion of nascent AMPA receptors (D_{app} : ER-GluA1, $0.038 \pm 0.004 \mu\text{m}^2/\text{s}$; ER-GluA2, $0.069 \pm 0.013 \mu\text{m}^2/\text{s}$; ER-VSVG, $0.081 \pm 0.004 \mu\text{m}^2/\text{s}$; SERCA2a, $0.092 \pm 0.009 \mu\text{m}^2/\text{s}$). Although slightly smaller than that of VSVG, the exchangeable fractions of GluA1 and GluA2 in the ER were quite high (ER-VSVG, $85 \pm 2\%$; ER-GluA1, $79 \pm 2\%$; ER-GluA2, $75 \pm 3\%$), indicating that most AMPA receptors are exchangeable and mobile in the ER (Figure 1E, bottom panel).

The measured recovery kinetics, mobile fractions, and apparent diffusion rates were comparable to those of receptors in the extrasynaptic plasma membrane (Ehlers et al., 2007) and mirrored the dynamics of the freely diffusing membrane proteins GT-46 and PM-phluo at the dendritic surface (Figures 1D and 1E and Table S1). Thus, mobility of nascent receptors in the ER is nearly as rapid as that of mobile receptors at the PM.

To directly examine the rate and spatial extent of ER membrane protein mobility throughout entire living neurons, we performed fluorescence loss in photobleaching (FLIP) experiments in neurons expressing ER-VSVG (Figure 1F). Continuous bleaching of the soma led to a progressive loss of dendritic fluorescence (Figures 1F and 1G and Figure S1L), demonstrating functional continuity of the somatodendritic ER. Whereas fluorescence loss occurred within minutes in proximal dendrites, distal dendrites were more slowly depleted and retained a significant fraction of their initial fluorescence (Figures 1F–1H). Thus, although highly mobile over micron scales, nascent receptors in the dendritic ER exhibit spatially restricted exchange over longer distances.

Membrane Cargo Mobility in the Dendritic ER Diminishes over Development

Although ER-VSVG appears diffuse in low-resolution FRAP experiments (Figure S1F and Figure S2G), super resolution structured illumination microscopy (SR-SIM) (Schermelleh et al., 2010) revealed subcellular heterogeneities in the dendritic ER (Figure 1I). Most neurons displayed clusters of increased fluorescence distributed along dendrites (Figure 1I), which were stable for many minutes (Figure 1J), and became more prominent over neuronal development (Figures 2A and 2B). Membrane protein mobility in the ER is likely restricted by structural features such as anastomoses and cisterns. Since these structures cannot be resolved by conventional fluorescence microscopy (Spacek and Harris, 1997), we developed a FRAP-based method to quantitatively assess diffusional restriction and ER complexity within local dendritic segments. We took advantage of the fact that the size of the bleached area affects fluorescence recovery rates (Sprague and McNally, 2005). Specifically, since the volume of any object increases with size faster than its surface area, increasing the size of the bleached area decreases the surface area to volume ratio and hence decreases the interface available for exchange of bleached and nonbleached molecules. Thus, for any exchanging molecule, measured recovery rates become progressively slower as a function of the effective complexity of the fluorophore-accessible volume as the size of the bleached area increases (Figure 2C and Figure S2). Hence, by comparing the ratio of fluorescence recovery after bleaching a large area to that after bleaching a small area, one obtains a functional measure of the effective complexity of the fluorophore-accessible volume (Figure S2).

Using this assay, we found that membrane protein mobility in the dendritic ER declines significantly over neuronal development (Figures 2C–2E). As the length of bleached dendritic segment was increased, the slowing of recovery times was more pronounced in older neurons (Figures 2D and 2E), indicating increased effective complexity (Figure 2C and Figure S2).

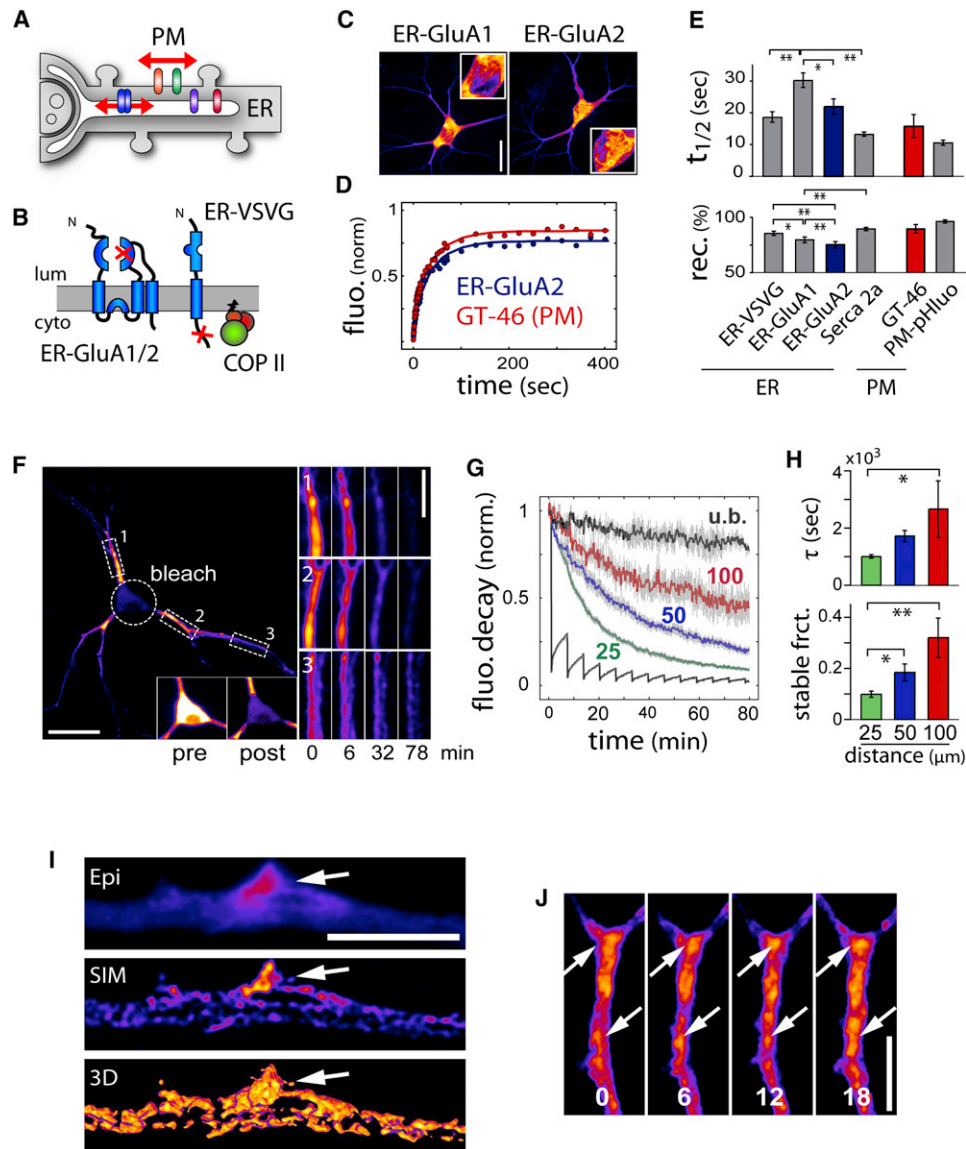


Figure 1. Membrane Protein Dynamics in the Dendritic ER

(A) Model illustrating the mobility of membrane proteins in the ER and at the surface of a neuronal dendrite. PM, plasma membrane.

(B) ER-retained GluA1 and GluA2 subunits (ER-GluA1/2) mimicking nascent receptors were generated by point mutation in the glutamate binding site (see also Figure S1). A constitutively ER-retained version of VSVG (ER-VSVG) was generated by mutagenesis of VSVG COPII binding motifs. Lum, lumen; cyto, cytosol. (C) Distribution patterns of ER-GluA1 and ER-GluA2 in DIV15 hippocampal neurons. Insets show higher magnification of cell bodies. The scale bar represents 30 μm .

(D) Examples of raw (filled circles) and fitted (lines) FRAP plots obtained for GluA2 in the ER (ER-GluA2) and GT46 at the plasma membrane (PM).

(E) Average recovery half-time ($t_{1/2}$) and fractional recovery measured for integral membrane proteins in the ER or at the cell surface (PM) in DIV17–22 neurons (see also Movie S1). Mean \pm SEM, $n = 64, 38, 28, 44, 14,$ and 22 cells, for ER-VSVG, ER-GluA1, ER-GluA2, SERCA2a, GT46, and PM-pHluo, respectively, three to four experiments each; * $p < 0.05$, ** $p < 0.01$; ANOVA.

(F) Loss of dendritic ER-VSVG fluorescence upon continuous bleaching of the soma. Time-lapse sequences are shown for proximal (1, 2) and distal (3) dendritic segments. Insets show ER-VSVG fluorescence before (pre) and after (post) photobleaching the soma. The scale bars represent 30 μm and 5 μm (inset).

(G) Fluorescence decay in the soma (gray) and in dendritic segments at 25 μm (green), 50 μm (blue), and 100 μm (red) from the soma in bleached neurons and at 100 μm from the soma in unbleached neurons (u.b., black). $n = 7$ –11 dendrites in 9 cells, three experiments.

(H) Decay constants (τ) and stable fractions in dendrites as a function of distance from the soma. Mean \pm SEM; * $p < 0.05$, ** $p < 0.01$; ANOVA.

(I) Super-resolution image of ER-VSVG obtained by structured illumination microscopy (SIM) showing spatial heterogeneities within the dendritic ER image. Epi, epifluorescence image; SIM, SIM image; 3D, 3D reconstruction. The scale bar represents 5 μm .

(J) Time-lapse sequence of ER-VSVG. Shown are z-stack projections illustrating the relative stability of ER spatial heterogeneities (arrows). Times are shown in minutes. The scale bar represents 5 μm .

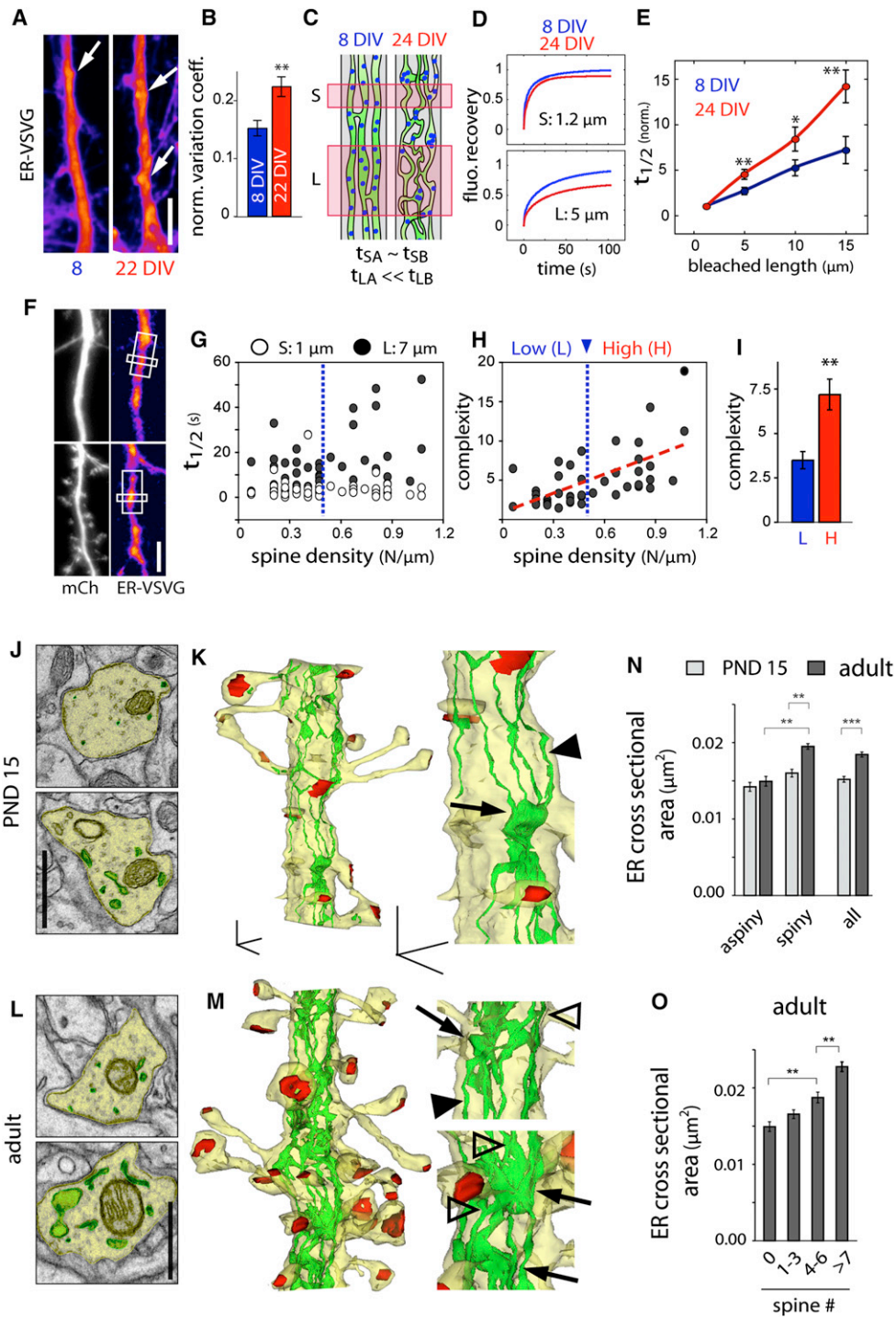


Figure 2. Increased ER Complexity and Reduced ER Mobility in Older Spiny Dendrites

(A and B) Distribution pattern (A) and variance (B) of ER-VSVG fluorescence along dendrites of young (DIV8–11, left) and older (DIV22, right) neurons. Arrows show spots of increased ER-VSVG intensity. Mean \pm SEM, $n = 13$; ** $p < 0.01$; t test. The scale bar represents 5 μ m.

(C and D) FRAP-based measurement of ER complexity (see also Figure S2). (C) Schematic of experimental approach. FRAP measurements in small dendritic segments (t_s) provide information on intrinsic molecular properties independent of ER geometry (e.g., freely diffusing fraction, binding kinetics, etc.). FRAP measurements in larger dendrite segments (t_L) depend on ER geometry and the fluorophore-accessible volume. (D) Fitted plots of ER-VSVG fluorescence recovery after bleaching small (S, 1.2 μ m) or large (L, 5 μ m) segments in young (DIV8, blue) and old (DIV24, red) neurons.

(E) Recovery half-times (normalized $t_{1/2}$) as a function of the length of bleached dendritic segments in young (blue) and older (red) neurons. Mean \pm SEM, $n = 20, 21$ cells in four experiments, respectively; * $p < 0.05$, ** $p < 0.01$; t test.

This restricted mobility in older neurons was not due to a heterogeneous distribution of ER-VSVG binding sites as recovered fractions and diffusion anomaly were identical in young and mature neurons (Figure S2J).

Zones of ER Confinement Localize Near Dendritic Spines and Dendritic Branch Points

To determine whether ER membrane protein mobility is reduced near excitatory synapses (Spacek and Harris, 1997), we measured FRAP recovery rates derived from small 1 μm ($t_{1/2,S}$) and larger 7 μm ($t_{1/2,L}$) dendritic segments (Figure 2F), and calculated an ER complexity index as the ratio between $t_{1/2,L}$ and $t_{1/2,S}$ obtained from DIV18 hippocampal neurons with varying spine densities. In contrast to $t_{1/2,S}$ which remained constant, $t_{1/2,L}$ increased with spine density (Figure 2G), resulting in a positive correlation between spine density and ER complexity (Figures 2H and 2I). To examine the ultrastructural organization of the ER over dendritic development and its spatial relationship with spines in vivo, we performed serial section 3D reconstruction in CA1 pyramidal neurons. We compared ER morphology in dendrites displaying varying spine densities in postnatal day 15 (PND15) or adult neurons. In aspiny segments of PND15 dendrites, ER consisted primarily of multiple elongated longitudinal tubules connecting regions of increased ER volume found near dendritic spines (Figures 2J and 2K). In older dendrites ER volume was overall more heterogeneous with more branched tubules and larger distended cisternae in zones of high spine density (Figures 2L and 2M). As an indirect metric for ER complexity, we assessed ER volume variation along dendrites by comparing ER cross-sectional area in aspiny and spiny dendritic segments with varying spine number (Figure S2K). Although ER cross-sectional area was higher in spiny dendrites both in PND15 and adult neurons, this difference was more pronounced in adult neurons due to higher spine density (Figure 2N), resulting in a globally increased ER complexity in adults (Figure 2N). In agreement with previous studies (Spacek and Harris, 1997), variation of ER volume along the dendritic shaft of adult neurons was tightly correlated with local spine density (Figure 2O), providing a structural basis for reduced membrane cargo mobility. Consistent with EM reconstructions where spines rarely contained ER (Figures 2K and 2M), fluorescence microscopy showed that ER complexity is not due to ER entry into spines (Figures S2L–S2N).

We next performed FRAP measurements at various locations along dendrites (Figure 3A). We found no quantitative difference in submicron diffusion rates or ER complexity ($t_{1/2,L} / t_{1/2,S}$) between proximal and distal dendritic segments (Figures 3B and 3C and Table S1). In contrast, ER complexity was significantly higher at dendritic branch points (BPs) (Figures 3B and 3C). Importantly, the increased complexity at BPs was specific for membrane proteins in the ER and was not observed at the cell-surface (Figure 3C).

The restricted mobility of ER membrane cargo at BPs was further supported by photoactivation experiments (Figures 3D–3G). Specifically, ER-VSVG-paGFP photoactivated in dendritic segments accumulated and dwelled for extended periods at flanking BPs (Figures 3D and 3E). Conversely, decay rates of photoactivated VSVG-paGFP measured in 15–30 μm dendritic segments flanked by and encompassing BPs were significantly slower than in straight dendritic segments (Figures 3F and 3G). Taken together, these data show that BPs act as diffusional traps restricting ER membrane protein mobility.

Compartmentalized Diffusion of Nascent AMPA Receptors in the Dendritic ER

To determine how lateral diffusion impacts the size of the dendritic domain explored by newly synthesized membrane cargo in the ER, we simulated the spread of GluA1 in dendrites (Figures S3) using measured and extrapolated diffusion coefficients (Table S2) derived from straight segments and dendritic BPs. Exploration maps obtained over a total duration of 12 hr assuming a constant rate of synthesis at a given location (e.g., BP), indicate that nascent AMPA receptors concentrate within dendritic subcompartments (Figures S3A and S3B and Movie S2). This accumulation occurred over hours and, by 12 hr, produced a nearly 10-fold increase in receptor density centered at the synthesis site. Compartmentalization was particularly marked in complex dendrites (Figures S3C and S3D), due largely to the reduced mobility at BPs. If the reduced diffusion at BPs was excluded, the size of explored dendritic domains was significantly increased (Figure S3D). The additive contribution of individual dendritic branches to nascent receptor confinement was further confirmed by simulations in dendritic templates with defined geometries (Figure S3E), where each bounding branch point induced a $\sim 20\%$ increase in local receptor concentration (Figure S3F). These data show that cargo mobility within the

(F) Images of hippocampal neurons (DIV15) expressing an mCherry cell fill (mCh, left) and ER-VSVG (right). White boxes illustrate the small (1 μm) and large (7 μm) bleached areas. The scale bar represents 5 μm .

(G) Fluorescence recovery halftimes ($t_{1/2}$) as a function of dendritic spine density after sequential bleaching of small 1 μm (S, open circles) and large 7 μm segments (L, filled circles) in older neurons (DIV17–19). $n = 42$ cells, three experiments.

(H) ER complexity index ($t_{1/2,L} / t_{1/2,S}$) as a function of dendritic spine density. The dashed red line indicates the linear fit. A cutoff for high (H) and low (L) spine density was set at 0.5 spines/ μm (dashed blue line).

(I) Mean complexity index of dendritic segments with low spine densities under (L, blue) or high spine densities above (H, red) 0.5 spines/ μm . Mean \pm SEM, $n = 17$, 25 cells in three experiments, respectively; * $p < 0.05$, ** $p < 0.01$; t test.

(J–M) Electron micrographs (J and L) and three-dimensional reconstructions (K and M) at low and higher magnification, showing the cytoplasm (J and L) or the plasma membrane ([K and M] yellow), the ER (green) and excitatory postsynaptic differentiations (red) in postnatal day 15 (PND 15 [J and K]) and adult (L and M) CA1 pyramidal neuron apical dendrites. Note the elongated longitudinal ER tubules (arrow heads), ER branching (empty arrow heads) and local increase of ER volume at the base of dendritic spines (arrows). In adult neurons, note the increased ER branching (empty arrowheads) and cisternae (arrows). The scale bar represents 1 μm (J and L), 500 nm (K and M).

(N and O) Average ER cross-sectional area in aspiny, spiny, and spiny plus aspiny segments (all [N]) of PND 15 or adult dendrites, and (O) correlation with spine number in adult dendrites. Mean \pm SEM, $n = 528$ –539 sections in PND 15 aspiny and spiny segments, and $n = 433$ –544 sections in adult aspiny and spiny segments, $n = 10$ –17 dendrites from 2–4 animals; ** $p < 0.01$, *** $p < 0.001$; ANOVA or t test.

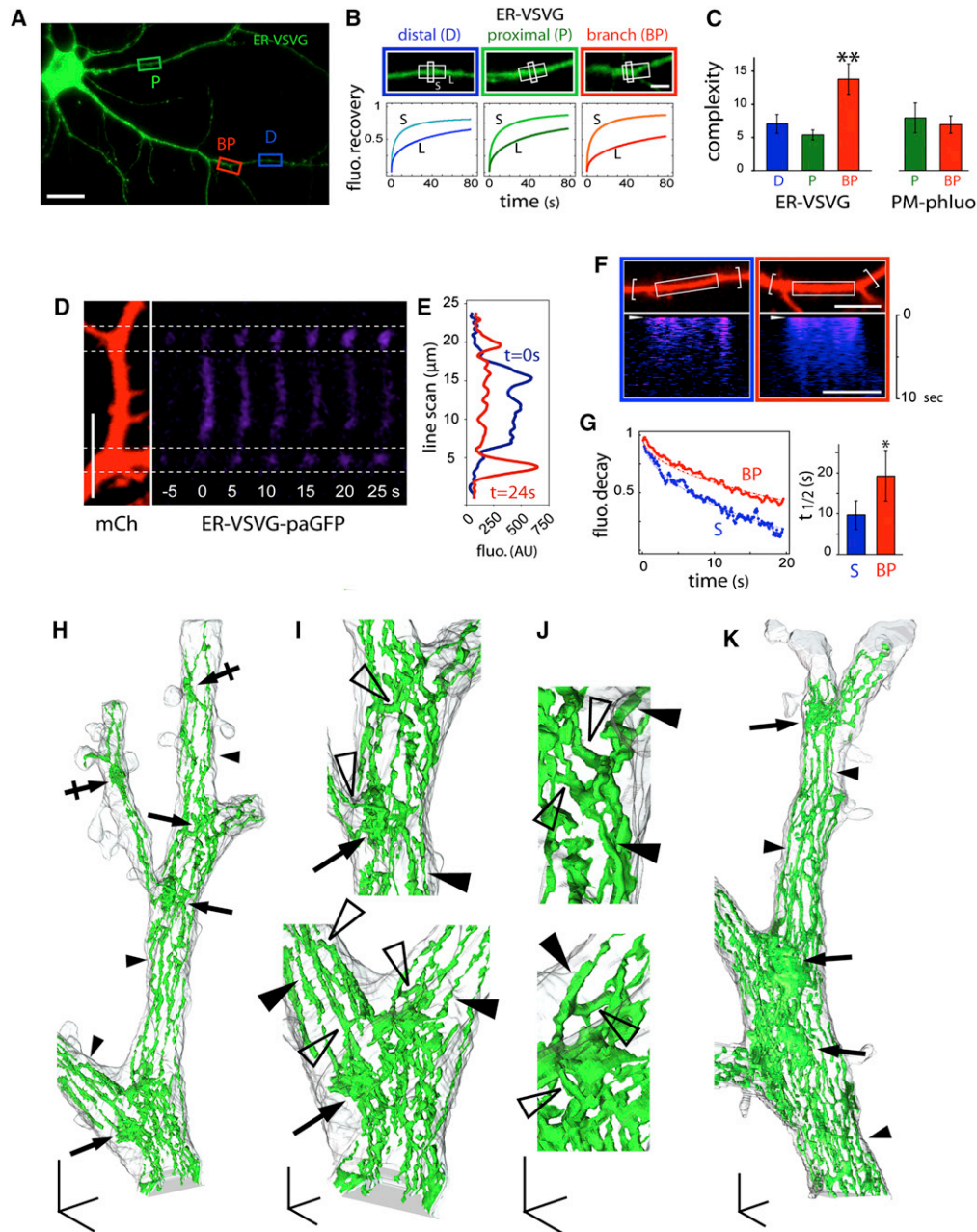


Figure 3. Diffusional Trapping of ER Membrane Cargo at Dendritic Branch Points

(A) ER-VSVG expression in a DIV15 hippocampal neuron. Shown are examples of proximal (P), distal (D), and branch point (BP) regions subjected to photo-bleaching. The scale bar represents 30 μm .

(B) Averaged FRAP plots obtained after sequential bleaching of small 1 μm (S, light colors) and large 7 μm dendritic segments (L, dark colors) in distal dendrites (D, blue), proximal dendrites (P, green), and dendritic BPs (red). The scale bar represents 5 μm .

(C) Average complexity ($t_{1/2, L} / t_{1/2, S}$) measured for ER-VSVG in the ER and PM-phluo at the plasma membrane (PM). D, distal; P, proximal; BP, branch point. Mean \pm SEM, $n = 12$ –18 cells in two to three experiments each; ** $p < 0.01$; ANOVA.

(D) Photoactivation of ER-VSVG-paGFP in a region of dendrite between two BPs. Photoactivated ER-VSVG-paGFP (blue, right) diffused away from the photoactivated region but was trapped at adjacent BPs. mCh was coexpressed as a cytosolic cell fill (left). The scale bar represents 10 μm .

(E) Line-scan of ER-VSVG-paGFP fluorescence at two time points following photoactivation.

(F) Photoactivation of ER-VSVG-paGFP in a straight dendritic segment (left, white box) or in a dendritic segment flanked by BPs (right, white box) (see also Figure S3 and Movie S2). Bottom panels show kymographs of fluorescence intensity along the dendrite. The scale bar represents 10 μm .

(G) Fluorescence decay plots (left) and average decay half times (right) following ER-VSVG-paGFP photoactivation measured in straight (S) dendritic segments or dendritic segments of equal length flanked by BPs. Fluorescence measurements were made from larger regions that encompassed BPs as indicated by the brackets in (F). Mean \pm SEM, $n = 10$ cells, three experiments; * $p < 0.05$; t test.

ER tunes the local reservoir of available nascent receptors and is strongly influenced by local dendritic geometry.

Increased ER Complexity and Preferential ER Export at Dendritic Branch Points

The increased diffusional confinement coupled with the unchanged short-range fluorescence recovery kinetics at BPs (Figure 3B) suggested local increase in the geometric complexity of ER structure. To address this, we performed serial section 3D reconstruction in CA1 pyramidal neurons. In straight segments of dendrite, the ER consisted of elongated longitudinal tubules connected by occasional transverse bridging tubules (Figures 3H and 3K). At BPs, ER was much more complex, with multiple anastomosing tubules and flattened cisternae (Figures 3H–3K), providing a structural basis for reduced membrane cargo mobility.

To test whether ER structural complexity corresponds to sites of secretory protein biosynthesis, we examined the distribution of ER-bound ribosomes and found that they are concentrated at dendritic BPs (Figure 4A). This suggests that BPs constitute a primary entry site of locally translated proteins into the secretory pathway. Indeed, FRAP experiments indicated a significant reduction in secretory cargo mobility in ER domains near Golgi outposts (GOs, Figure 4B), which are themselves concentrated at BPs (Horton et al., 2005; Ye et al., 2007). Moreover, ER-exit sites (ERES) marked by Sec23-immunolabeling were enriched at BPs and locally clustered around GOs (Figure 4C). This suggests that local ER complexity facilitates local export and processing of secretory cargo. To investigate this, we imaged VSVGts045, a model cargo that can be released from the ER in a thermosensitive manner, to monitor synchronized cargo progression in the secretory pathway (Horton and Ehlers, 2003). Following release from the ER, VSVGts rapidly accumulated at BPs (Figures 4D and 4E and Figures S4A and S4B), leading in turn to a rapid and local increase of Sec23 (Figures 4E and 4F), indicative of local ER export (Figure S4C; Farhan et al., 2008). These data demonstrate a spatial correlation between increased ER complexity, decreased cargo mobility, and preferential ER export at BPs.

We then sought to determine whether zones of increased ER complexity correspond to sites of secretory exocytosis. We took advantage of the transcytotic itinerary of the presynaptic protein VAMP2, which is first exocytosed in dendrites, internalized, and then targeted to and enriched in axon terminals (Sampo et al., 2003), allowing clear spatial segregation of exocytosis from secretory and endosomal compartments. In parallel with VSVGts release from the ER, secretory exocytosis of super-ecliptic-GFP tagged VAMP2 (VAMP2-SEP) occurred preferentially at BPs (Figures 4G–4I and Movie S3).

Acute Regulation of Dendritic ER Complexity by an mGluR/PKC/CLIMP63 Pathway

The developmental increase in dendritic ER complexity and its correlation with dendritic spine density (Figure 2) suggested

regulation by emergent synaptic activity. This prompted us to assess whether activation of postsynaptic glutamatergic receptors controls ER morphology and effective complexity. In dendrites where ER fine structure could be well-resolved, ER-localized membrane cargo was noticeably less uniform and concentrated in ER nodules following activation of group I metabotropic glutamate receptors (mGluRs) using the selective agonist (S)-3,5-dihydroxyphenylglycine (Figures 5A–5C). As confirmed by super-resolution imaging, these structures correspond to regions of convoluted ER (Figure 5B). Although these nodules were clearly visible only in ~60% of neurons at diffraction-limited resolution, DHPG increased fluorescence variation along dendrites regardless of nodule appearance (Figure 5C). Correspondingly, DHPG caused a significant increase in dendritic ER complexity measured by FRAP (Figures 5D–5F), whereas NMDA receptor activation had no effect on this parameter. The mGluR-induced increase in ER complexity occurred without measurable ER stress (Figure S5) and mGluR activation did not change submicron diffusion rates (Figures 5D and 5E and Table S1), indicating that the effect was not due to a compositional change in the ER. The group I mGluRs (mGluR1, mGluR5) couple to G_q and thereby trigger protein kinase C (PKC) and inositol 1,4,5-trisphosphate (IP3)-dependent signaling pathways. Correspondingly, the DHPG-induced increase in ER morphological and effective complexity was abolished by inhibiting PKC (Figures 5C and 5F). The effect of mGluR activation was not cargo selective, as the apparent diffusional complexity index for both ER-VSVG and ER-GluA1 was increased to the same extent (Figure 5F) despite different absolute mobilities (Figure 1E). Thus, postsynaptic mGluR signaling via PKC rapidly confines nascent receptor diffusion in the dendritic ER.

In fibroblasts, ER interaction with microtubules is an important determinant of ER morphology (Vedrenne and Hauri, 2006). We thus examined ER ultrastructure in vivo and found that whereas elongated ER tubules frequently contacted microtubules (Figure 6A), convoluted ER membranes seen at BPs were much more loosely associated with microtubules (Figures 6A and 6B). Among the potential targets of PKC at the ER, CLIMP63 is an ER integral membrane protein whose binding to microtubules is regulated by PKC-dependent phosphorylation (Klopfenstein et al., 1998; Schweizer et al., 1993; Vedrenne et al., 2005). When bound to microtubules in fibroblasts, CLIMP63 promotes elongation of ER tubules to the cell periphery along microtubule tracts (Klopfenstein et al., 1998; Vedrenne et al., 2005). Phosphorylation of one or more N-terminal serine residues (S3, S17, and S19) abrogates microtubule binding (Figure 6C), eventually resulting in ER collapse and membrane stacking around the nucleus (Vedrenne et al., 2005). CLIMP63 is highly expressed in brain (Farah et al., 2005), and given the regulation of dendritic ER complexity by mGluR/PKC (Figure 5), we wondered whether the increased ER complexity seen in neurons after mGluR activation involved CLIMP63 phosphorylation. To test this, we generated phosphodeficient (CLIMP63-S3A, S17A, S19A; referred to

(H–K) Three-dimensional reconstructions of electron micrographs showing the plasma membrane (gray) and the ER (green) at different magnifications. Note the presence of ER cisternal sheets at dendritic BPs (arrows) and the extensive branching of the ER membrane (bridging tubules, empty arrowheads), contrasting with ER tubules (filled arrowheads) in straight dendritic segments. The morphological complexity of the ER was also increased in areas with high spine density (crossed arrows in [H]). The scale bars represent 1 μ m (H and K), 500 nm (I), and 250 nm (J).

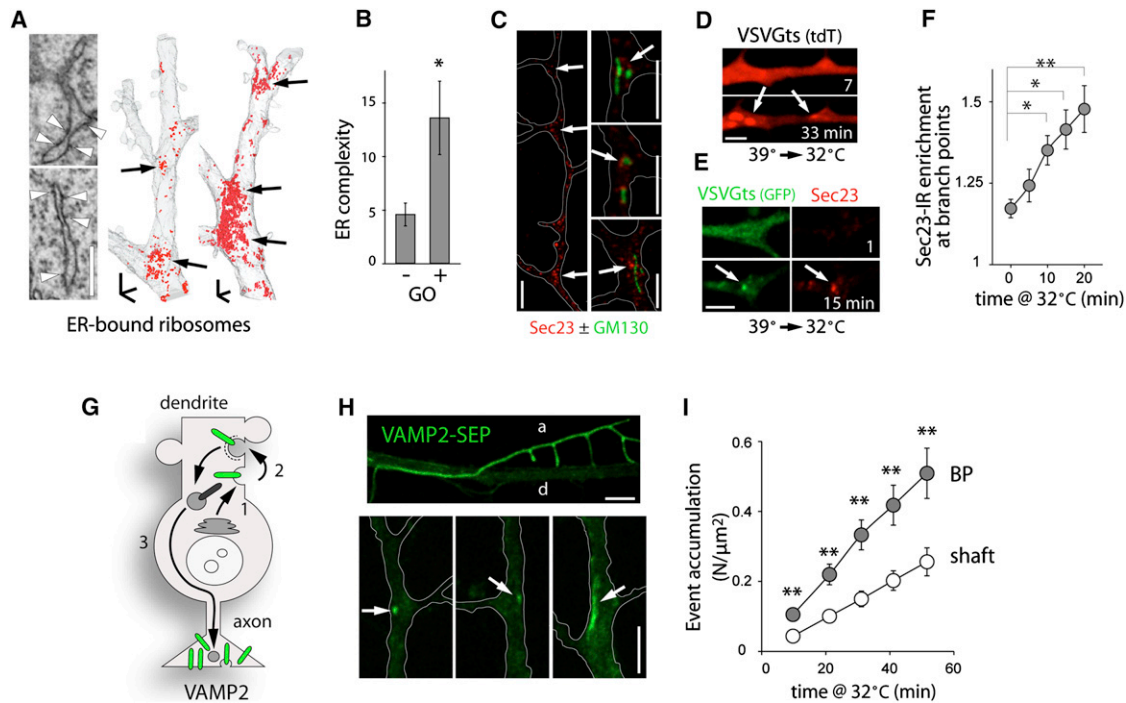


Figure 4. Preferential ER Entry and ER Exit at Dendritic Branch Points

(A) Three-dimensional EM reconstructions showing ER-bound ribosome distribution in segments of CA1 dendrites. Note the concentration of ER-bound ribosomes at BPs (arrows). The scale bar represents 1 μm . (B) ER complexity index in dendritic segments lacking (-) or containing (+) Golgi outposts (GOs). Mean \pm SEM, $n = 10$ cells in two experiments; * $p < 0.05$; t test. (C) Sec23 immunoreactivity showing the distribution of ER exit sites in dendrites of DIV7 neurons. The scale bars represent 5 μm . (D) Accumulation of VSVGs at BPs (arrows) 7 and 33 min after temperature-induced release of ER exit blockade (39°C to 32°C shift) (see also Figure S4). The scale bar represents 5 μm . (E–F) Images (E) and quantification (F) of the preferential increase of Sec23 at BPs after VSVGs release from the ER by shift to 32°C. The scale bar represents 5 μm . Mean \pm SEM, $n = 8$ –24 cells, two to four experiments for each; * $p < 0.05$, ** $p < 0.01$; ANOVA. (G–I) Preferential exocytosis at BPs (see also Movie S3). (G) VAMP2 is first secreted in the somatodendritic membrane (1), internalized (2) and subsequently targeted to the axon (3). (H) VAMP2-SEP fluorescence in a dendrite and an axon (*d* and *a*, upper) and discrete exocytosis events at BPs (arrows, lower). The scale bar represents 5 μm . (I) Cumulative exocytosis events at BPs and in the dendritic shaft. Mean \pm SEM, $n = 30$ dendrites in 15 neurons; * $p < 0.05$, ** $p < 0.01$; ANOVA.

as 3A) and phosphomimetic (S3E, S17E, S19E; referred to as 3E) mutant forms of CLIMP63 that either strongly bind (3A) or fail to bind (3E) microtubules (Vedrenne et al., 2005). In neurons, CLIMP63-3A was uniformly distributed in straight tubular structures throughout dendrites (Figure 6D, Figure S6B, and Movie S4), consistent with tight microtubule binding. In contrast, phosphomimetic CLIMP63-3E was present in nonuniform clusters (Figure 6D, Figure S6B, and Movie S4), consistent with a decreased binding to microtubules. The ER in neurons expressing CLIMP63-3E was still present throughout dendrites (Figure S6B), but became much more convoluted (Figure 6D and Movie S4), similar to changes in the ER observed upon mGluR activation (Figure 5B).

Along with changes in ER morphology (Figure 6D), expression of CLIMP63-3E significantly increased ER diffusional complexity in the dendritic shaft (Figure 6E). Conversely, expression of CLIMP63-3A decreased ER complexity in the shaft (Figure 6E). Notably, the increased ER complexity at BPs was abrogated by CLIMP63-3A but was not further increased by CLIMP63-3E (Figure 6E). These effects on ER effective complexity occurred with

minor modifications in the local, absolute mobility of ER-VSVG (Table S1). Consistently, knockdown of endogenous CLIMP63 by RNA interference (RNAi) phenocopied the effect of CLIMP63-3E (Figures 6F–6H and Figure S6C). Moreover, whereas CLIMP63-3A blocked the DHPG-induced increase in ER effective complexity, CLIMP63-3E quantitatively occluded the effect (Figure 6I). In addition to normalizing ER complexity between BPs and adjacent dendritic shaft, expression of CLIMP63-3A abolished the preferential ER export of cargo at BPs induced by acute ER release of VSVGs (Figure 6J; compare to Figure 4F). These data provide strong evidence that mGluR signaling increases ER complexity and reduces nascent receptor mobility via PKC-dependent phosphorylation of CLIMP63.

Endoplasmic Reticulum Complexity Regulates Dendritic Morphogenesis and Synaptic Strength

Previous studies identified dendritic GOs as hubs for forward secretory trafficking, locally providing membrane components to growing dendrites (Horton et al., 2005; Ye et al., 2007). Whether and how nascent secretory cargo is confined within

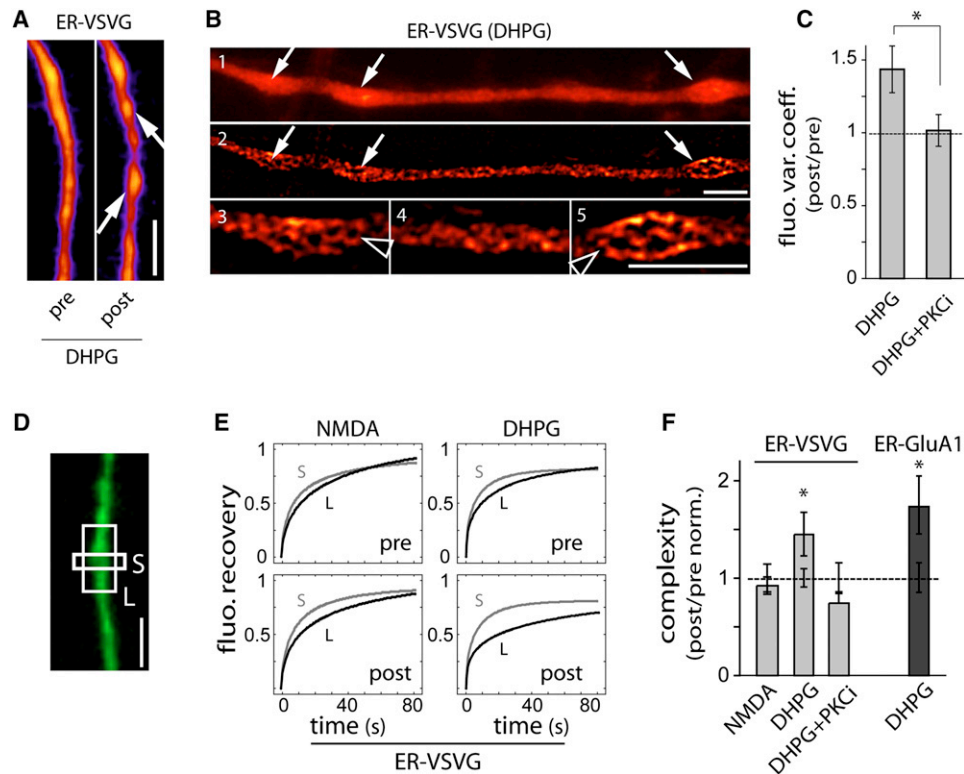


Figure 5. Group I mGluR Signaling Modifies ER Morphology and Reduces ER Cargo Mobility

(A) Increased heterogeneity of ER-VSVG distribution after a 30 min exposure to DHPG (arrows) (see also Figure S5). The scale bar represents 5 μ m. (B) Structured illumination microscopy images of a dendrite showing ER-VSVG fluorescence before (1) and after SIM imaging (2–5) at low (1–2) and higher (3–5) magnifications. Note the extensive branching (arrowheads) of ER membranes in DHPG-induced nodules (arrows). The scale bar represents 5 μ m. (C) Increased variation in ER-VSVG fluorescence along dendrites in cells as shown in (A) in the absence (DHPG) or presence of a PKC inhibitor (PKCi, 100 nM bisindolylmaleimide). Data are normalized to values measured prior to drug application, Mean \pm SEM. DHPG, n = 7; DHPG + PKC inhibitor, n = 8 cells; one to two experiments each; *p < 0.05; t test. (D and E) Representative FRAP plots obtained from sequential bleachings of small 1 μ m (S, gray) and large 7 μ m (L, black) dendritic segments (DIV14) before (pre) and after (post) exposure to NMDA or DHPG. (F) Effective complexity ($t_{1/2, L} / t_{1/2, S}$) in individual dendrites exposed to NMDA, DHPG and DHPG + PKCi. ER complexity values measured by FRAP following stimulation with indicated reagents are normalized to values measured prior to drug application (PKCi, 100 nM bisindolylmaleimide), Mean \pm SEM n = 34, 42, 16 cells for ER-VSVG in NMDA, DHPG, and DHPG + PKCi treatment, respectively; n = 19 cells for ER-GluA1 in DHPG treatment; two to four experiments; *p < 0.05 (relative to 1.0); t test.

the dendritic ER has been unclear. To address this, we first used CLIMP63-3E as a marker for zones of complex ER (Figure 6). In DIV 7 neurons, a period of intense dendritic growth and remodeling (Horton et al., 2005), CLIMP63-3E was concentrated at BPs (Figure 7A). This local concentration was correlated with the emergence and growth of new dendritic branches (Figures 7B and 7C and Figure S7A). 72% \pm 9% of CLIMP63-3E clusters in primary dendrites (n = 40 in 6 neurons) corresponded to sites of new branch formation, suggesting that local zones of increased ER complexity promote dendritic branching. To address this further, we measured the effect of CLIMP63 mutants on the morphology of pyramidal neuron primary dendrites, whose growth and morphology is tightly coupled to secretory trafficking (Horton et al., 2005). Expression of CLIMP63-3A resulted in fewer proximal branches (Figures 7D–7F). In contrast, expression of CLIMP63-3E triggered a large increase in dendritic branching (Figures 7D–7F). Moreover, RNAi knockdown of CLIMP63 (Figure 7G) phenocopied the effect of CLIMP63-3E

(Figures 7H and 7I). The increase in dendritic branching induced by CLIMP63 knockdown was reversed by expression of CLIMP63-3A (Figures 7H and 7I).

In addition, we sought to determine whether ER complexity controls the abundance of AMPA receptors at the dendritic plasma membrane. Compared to CLIMP63-3A, CLIMP63-3E expression increased both surface and synaptic GluA1 (Figures S7B and S7C). Moreover, Whole-cell patch-clamp recordings revealed increased amplitude and frequency of miniature excitatory postsynaptic currents (mEPSCs) in neurons expressing CLIMP63-3E (Figures S7D and S7E). These data show that increases in ER complexity produce corresponding increases in surface and synaptic levels of AMPA receptors.

DISCUSSION

The complex cellular geometry determines the computational properties of neurons (Spruston, 2008) and requires highly

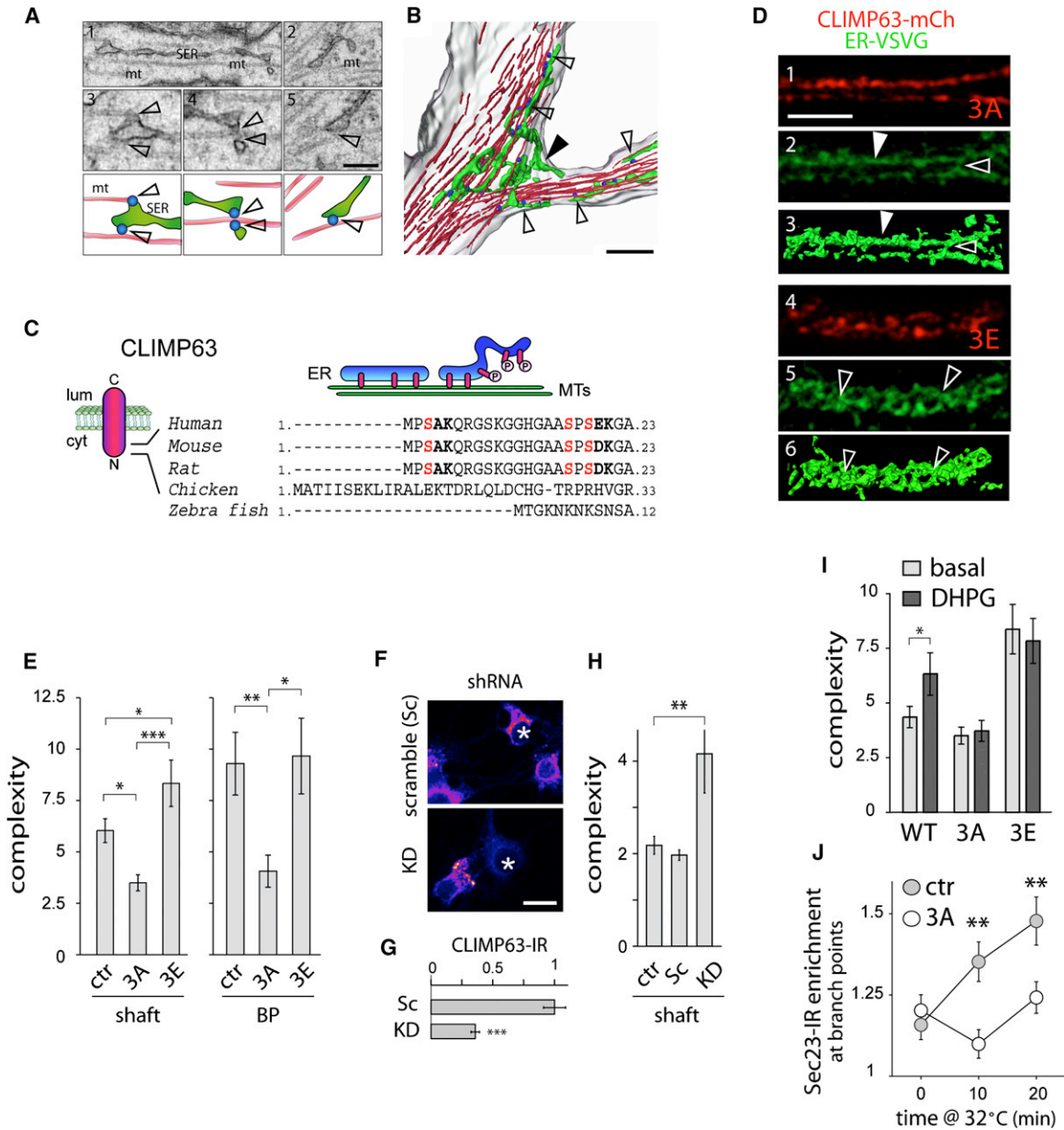


Figure 6. Phosphorylation-Dependent Binding of CLIMP63 to Microtubules Controls ER Morphology and Cargo Mobility

(A and B) Three-dimensional reconstructions of electron micrographs (A) showing the plasma membrane (gray), ER (green), microtubules (MT, red) and ER-MT contacts (blue) at a dendritic branch point (B). The scale bars represent 500 nm. In (B), note the looser association of bunched ER membranes (filled arrowhead) at the branch point compared to elongated tubules aligned with MTs in the dendritic shaft (empty arrowheads).

(C) Topology of CLIMP63 in the ER membrane (left) and regulation of ER microtubule binding by phosphorylation (right). Three serine residues in the N-terminus whose mutation prevents PKC-dependent phosphorylation are shown (red). Numbers indicate amino acids. Lum, lumen; cyt, cytosol.

(D) Super-resolution imaging of ER-VSVG (green) and CLIMP63-S3A, S17A, S19A (3A) or CLIMP63-S3E, S17E, S19E (3E) (red) in hippocampal neuron dendrites (DIV15) (see also Figure S6 and Movie S4). Elongated tubules (arrowheads) or branched ER membranes (empty arrowheads) are indicated. Three-dimensional surface renderings (3, 6) were derived from ER-VSVG images (2, 5). The scale bar represents 5 μ m.

(E) Apparent ER complexity measured by FRAP in the dendritic shaft or at BPs in neurons (DIV13-14) coexpressing ER-VSVG with either mCherry (ctr), mCh-CLIMP63-3A (3A), or mCh-CLIMP63-3E (3E). Mean \pm SEM, n = 64, 39 and 43 cells for dendritic shaft, n = 18, 14, 9 cells for BPs, respectively, four to five experiments for each; *p < 0.05, ***p < 0.01; ANOVA.

(F–G) CLIMP63 knockdown by RNA interference. (F) CLIMP63 immunoreactivity (IR, pseudocolored fluorescence) in untransfected and transfected (asterisks) neurons (somatas) expressing scramble (Sc) or target (KD) short hairpin RNAs (shRNA). (G) Normalized CLIMP63 levels in Sc and KD dendrites, Mean \pm SEM n = 19 cells, two experiments; ***p < 0.001; t test.

(H) CLIMP63 knockdown increases ER complexity. FRAP as in (E) in dendrites of neurons expressing scrambled (Sc) or CLIMP63 (KD) shRNAs or reporter only (tdTomato, ctr) with ER-VSVG. Mean \pm SEM, n = 25, 16 and 17 cells, respectively, three to five experiments for each; **p < 0.01; ANOVA.

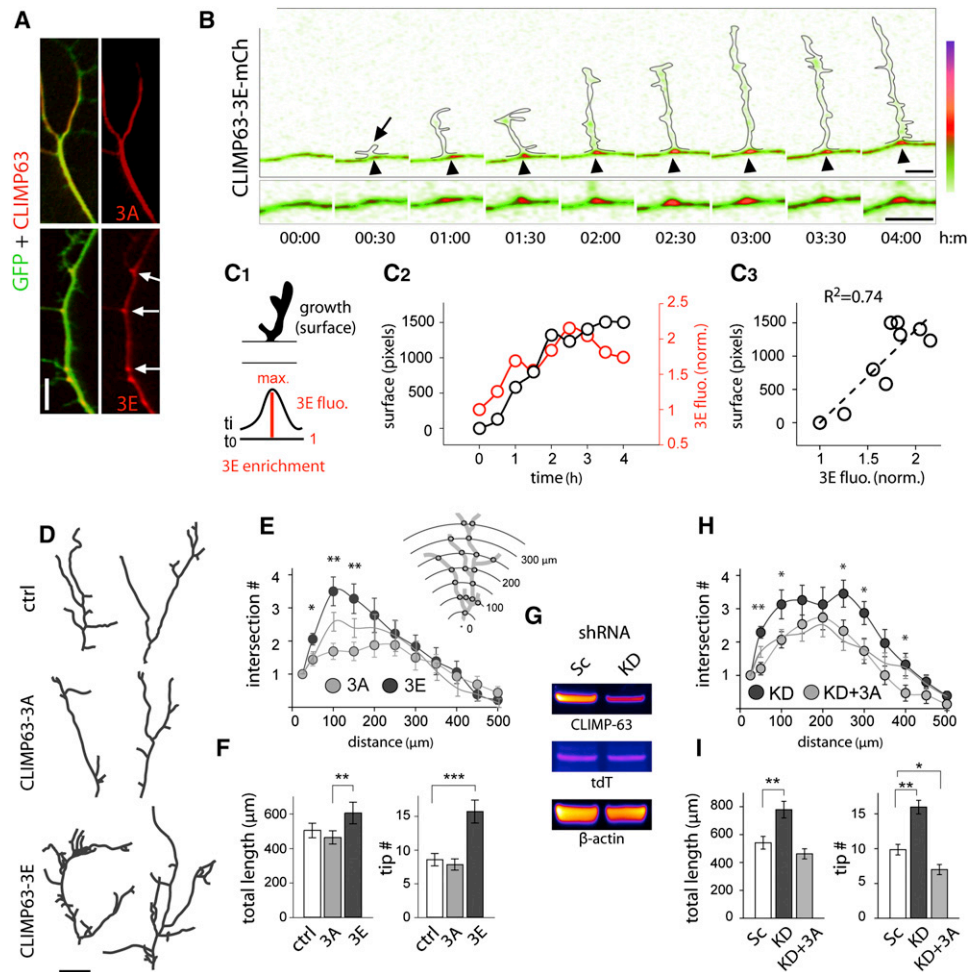


Figure 7. Phosphorylation of CLIMP63 Regulates Dendritic Branching

(A) Distribution of mCherry-tagged CLIMP63-3A and CLIMP63-3E (red) in DIV10 neurons expressing GFP (green). Note CLIMP63-3E enrichment at BPs (arrows). The scale bar represents 5 μ m.

(B) Zones of ER complexity labeled by CLIMP63-3E concentrate at sites of new dendritic branches (arrow) (see also Figure S7). Outlines represent GFP expressing emerging dendritic branch. Time in hr:min. The scale bar represents 5 μ m.

(C) CLIMP63-3E clustering precedes and marks sites of dendritic branching. Schematic of method to quantify dendritic branch growth and CLIMP63-3E enrichment index (C1), their variation with time (C2) and correlation (C3) after emergence of the branch shown in (B).

(D and E) Camera lucida drawings (D) and Sholl analysis (E) of primary dendrites from DIV10 hippocampal pyramidal neurons expressing mCherry (ctrl), CLIMP63-3A (3A), or CLIMP63-3E (3E). The scale bar represents 5 μ m. Mean \pm SEM, n = 16–18 cells, two experiments for each; *p < 0.05, **p < 0.01; t test (3A versus 3E).

(F) Primary dendrite length (μ m) and branch tip numbers for neurons expressing mCherry (ctrl), CLIMP63-3A (3A), or CLIMP63-3E (3E). Mean \pm SEM, ***p < 1×10^{-4} ; ANOVA.

(G) CLIMP63 knockdown after viral transduction. Shown are immunoblots for endogenous CLIMP63, tdTomato (tdT) and β -actin from hippocampal culture lysates after transduction with scramble (Sc) or CLIMP63 (KD) shRNA.

(H and I) Sholl analysis (H) and length and tip numbers (I) of primary dendrites from DIV10 hippocampal neurons. Neurons were transduced with scrambled (Sc) or CLIMP63 (KD) shRNA with or without an RNAi resistant mCherry-tagged CLIMP63-3A (3A). Mean \pm SEM, n = 15–31 cells, two to four experiments for each; *p < 0.05, **p < 0.01; t test (H) or ANOVA (I).

compartmentalized delivery of membrane cargo (Kennedy and Ehlers, 2006). In *Drosophila* oocytes, the range of ER diffusion dictates the location of cargo secretion and is crucial for polarized signaling (Herpers and Rabouille, 2004). In mammalian

neurons, dendritic spines act as diffusion sinks restricting cytoplasmic protein diffusion (Santamaria et al., 2006). In both cases, geometric complexity produces functional compartmentalization without direct immobilization. Our results suggest that

(I) CLIMP63-3A blocks and CLIMP63-3E occludes the DHPG-induced increase in ER complexity. Mean \pm SEM, n = 44, 39 and 43 cells, respectively, four to five experiments for each; *p < 0.05; t test.

(J) CLIMP63-3A abrogates the preferential increase of Sec23 at BPs after VSVGts release from the ER. The scale bar represents 5 μ m. Mean \pm SEM, n = 11–18 cells, two experiments for each; **p < 0.01; t test. Ctrl, control.

nascent secretory proteins in dendrites are confined by local ER complexity near spines and BPs, directly coupling organelle structure to dendritic geometry for local control of membrane production and composition.

Local synthesis of membrane proteins has been proposed to mediate diverse forms of neuronal plasticity. However, the spatial range with which locally synthesized receptors modify synapses is not clear. Newly synthesized GluA1 and GluA2 reach the Golgi apparatus with time constants of ~ 3 hr and ~ 12 hr, respectively (Greger et al., 2002). Such variable and prolonged dwell time in the ER is characteristic of multisubunit receptors and neuronal ion channels, and suggests the potential for tight regulation of ER export kinetics which, together with lateral ER diffusion, will determine the spatial range over which ER export occurs. Here, we have shown that the overall geometry and complexity of ER membranes can restrict the spatial mobility of membrane cargo near spines and BPs, providing a general mechanism to tune the spatial dimensions of secretory trafficking independent of cargo identity. Our results further show that increased ER complexity promotes AMPA receptor surface expression and accumulation at synapses, providing a potential basis for dendritic segment-specific variation in AMPA receptor abundance (Nicholson et al., 2006).

Group I mGluR activation promotes the dendritic accumulation of AMPA receptor subunit mRNAs (Grooms et al., 2006), increases dendritic ER-export (Aridor et al., 2004), and triggers the dendritic translation of AMPA receptors (Mameli et al., 2007). Here, we have shown that mGluR activation reduces the lateral mobility of nascent receptors by increasing ER complexity. Such a mechanism provides a pathway that couples local secretory processing of nascent receptors with signaling events controlling protein translation.

Extending for hundreds of microns, it has been unclear how the ER is elaborated in dendrites, what controls its structure or morphology, and how ER morphology impacts neuronal development and function. Here, we have shown that bidirectional regulation of ER complexity through CLIMP63 phosphorylation provides a direct mechanism to tune the spatial dimensions of ER cargo mobility in dendrites. Notably, the concentration of complex ER domains at dendritic BPs is accompanied by enrichment of ribosomes, ER exit sites, and GOs. This shows that the entire ensemble of secretory machinery becomes compartmentalized at BPs, and indicates that zones of increased ER complexity control dendritic branching by facilitating nascent cargo confinement and ER-export at sites of new branch formation.

Ultimately, spatially directed secretion together with retention of receptors and other secretory cargo in dendritic subdomains could both acutely augment and persistently confine new molecular components for locally modifying dendrite function. More broadly, local regulation of ER complexity may provide a general paradigm for stimulus-dependent regulation of local membrane composition in geometrically complex cells.

EXPERIMENTAL PROCEDURES

Cell Culture, Transfection, and shRNA Knockdown of CLIMP63

Rat hippocampal cultures were derived from E18 rat embryos and transfected as previously described (Horton and Ehlers, 2003). FRAP and photoactivation experiments were performed 12–24 hr posttransfection in neurons displaying

low to moderate levels of exogenous protein expression. For shRNA knockdown of CLIMP63, the sequence UCAACCGUAAUAGUGAAGUUCUACA was cloned in pLentilox3.7 and expressed for 5 to 10 d.

Live Cell Imaging and Drug Treatments

Hippocampal neurons were monitored at 37°C in E4 medium (150 mM NaCl, 3 mM KCl, 15 mM glucose, 10 mM HEPES, [pH 7.4]) supplemented with 2 mM CaCl₂, 2 mM MgCl₂ (standard E4) or 4 mM CaCl₂, 0 mM MgCl₂ (low Mg E4), for a maximal duration of 90 min. DHPG, TTX, NMDA, and AP5 (Tocris) were used at final concentrations of 100 μ M, 2 μ M, 50 μ M and 100 μ M, respectively. ER complexity was measured by FRAP analysis in low Mg E4 before and 25–35 min after addition of DHPG, or in low Mg E4 supplemented with TTX before and 15–30 min after a 3 min exposure to NMDA (Ehlers, 2000). The PKC inhibitor bisindolylmaleimide I (Calbiochem) was used at 100 nM. The 39° to 32°C and 39°–20°–32°C temperature-shift experiments with VSVGts045 were done as previously described (Horton and Ehlers, 2003).

Computational Analysis of ER Diffusion

Fluorescence recovery in dendrite segments was analyzed using a custom three-dimensional anomalous diffusion model. The diffusion of photoactivated molecules was quantified using the same model. For fluorescence loss in photobleaching (FLIP) experiments, fluorescence decay was quantified using monoexponential curve fitting after correction for photobleaching during imaging acquisition, which was determined on nearby unbleached dendrites.

Serial Section Electron Microscopy, 3D Reconstructions, and Analysis

Serial electron micrographs (EM) were obtained from the stratum radiatum in the CA1 area of male rat hippocampus as previously described (Spacek and Harris, 1997). The RECONSTRUCT™ software (Fiala and Harris, 2001) was used to align, reconstruct, quantify and visualize SER within the three-dimensional dendrite reconstructions using previously described identification criteria (Spacek and Harris, 1997).

ER cross sectional area in aspiny or spiny dendrites was calculated as the average of total cross-sectional ER area per section through spans of serial sections beginning with the first section where the base of a spine started to emerge and ended with the section where the base of the last spine was no longer detectable (Figure S2K). A dendritic segment was considered aspiny if it spanned two or more serial sections without a spine emerging.

Super-Resolution Imaging

Structured illumination fluorescence imaging was performed using a 63 \times 1.4 NA objective on a Zeiss Super resolution-SIM inverted microscope (Carl Zeiss, Inc.). 3D reconstructions were generated in Amira (Visage Imaging, Inc.).

SUPPLEMENTAL INFORMATION

Supplemental Information includes Extended Experimental Procedures, two tables, seven figures, and four movies and can be found with this article online at doi:10.1016/j.cell.2011.11.056.

ACKNOWLEDGMENTS

We thank Ben Arenkiel, Ian Davison, Juliet Hernandez, Matt Kennedy, Tom Newpher, and Rui Peixoto for critical reading of the manuscript. We thank Larry Lindsey and Cam Robinson for help with EM data processing. We thank Irina Lebedeva and Marguerita Klein for technical assistance. We thank Zeiss USA for use of their structured illumination microscopy system. Work in the laboratory of M. D. E. was supported by NIH grants NS039402, MH064748, and MH086339, and the Howard Hughes Medical Institute. Work in the laboratory of K.M.H. is supported by NIH grants NS021184 and EB002170.

Received: February 18, 2010

Revised: March 28, 2011

Accepted: November 17, 2011

Published: January 19, 2012

REFERENCES

- Aridor, M., Guzik, A.K., Bielli, A., and Fish, K.N. (2004). Endoplasmic reticulum export site formation and function in dendrites. *J. Neurosci.* *24*, 3770–3776.
- Cooney, J.R., Hurlburt, J.L., Selig, D.K., Harris, K.M., and Fiala, J.C. (2002). Endosomal compartments serve multiple hippocampal dendritic spines from a widespread rather than a local store of recycling membrane. *J. Neurosci.* *22*, 2215–2224.
- Ehlers, M.D. (2000). Reinsertion or degradation of AMPA receptors determined by activity-dependent endocytic sorting. *Neuron* *28*, 511–525.
- Ehlers, M.D., Heine, M., Groc, L., Lee, M.C., and Choquet, D. (2007). Diffusional trapping of GluR1 AMPA receptors by input-specific synaptic activity. *Neuron* *54*, 447–460.
- Farah, C.A., Liazoghli, D., Perreault, S., Desjardins, M., Guimont, A., Anton, A., Lauzon, M., Kreibich, G., Paiement, J., and Leclerc, N. (2005). Interaction of microtubule-associated protein-2 and p63: a new link between microtubules and rough endoplasmic reticulum membranes in neurons. *J. Biol. Chem.* *280*, 9439–9449.
- Farhan, H., Weiss, M., Tani, K., Kaufman, R.J., and Hauri, H.P. (2008). Adaptation of endoplasmic reticulum exit sites to acute and chronic increases in cargo load. *EMBO J.* *27*, 2043–2054.
- Fiala, J.C., and Harris, K.M. (2001). Extending unbiased stereology of brain ultrastructure to three-dimensional volumes. *J. Am. Med. Inform. Assoc.* *8*, 1–16.
- Fukatsu, K., Bannai, H., Zhang, S., Nakamura, H., Inoue, T., and Mikoshiba, K. (2004). Lateral diffusion of inositol 1,4,5-trisphosphate receptor type 1 is regulated by actin filaments and 4.1N in neuronal dendrites. *J. Biol. Chem.* *279*, 48976–48982.
- Gardiol, A., Racca, C., and Triller, A. (1999). Dendritic and postsynaptic protein synthetic machinery. *J. Neurosci.* *19*, 168–179.
- Greger, I.H., Khatri, L., and Ziff, E.B. (2002). RNA editing at arg607 controls AMPA receptor exit from the endoplasmic reticulum. *Neuron* *34*, 759–772.
- Grooms, S.Y., Noh, K.M., Regis, R., Bassell, G.J., Bryan, M.K., Carroll, R.C., and Zukin, R.S. (2006). Activity bidirectionally regulates AMPA receptor mRNA abundance in dendrites of hippocampal neurons. *J. Neurosci.* *26*, 8339–8351.
- Hanus, C., and Ehlers, M.D. (2008). Secretory outposts for the local processing of membrane cargo in neuronal dendrites. *Traffic* *9*, 1437–1445.
- Herpers, B., and Rabouille, C. (2004). mRNA localization and ER-based protein sorting mechanisms dictate the use of transitional endoplasmic reticulum-golgi units involved in gurken transport in *Drosophila* oocytes. *Mol. Biol. Cell* *15*, 5306–5317.
- Horton, A.C., and Ehlers, M.D. (2003). Dual modes of endoplasmic reticulum-to-Golgi transport in dendrites revealed by live-cell imaging. *J. Neurosci.* *23*, 6188–6199.
- Horton, A.C., Racz, B., Monson, E.E., Lin, A.L., Weinberg, R.J., and Ehlers, M.D. (2005). Polarized secretory trafficking directs cargo for asymmetric dendrite growth and morphogenesis. *Neuron* *48*, 757–771.
- Kennedy, M.J., and Ehlers, M.D. (2006). Organelles and trafficking machinery for postsynaptic plasticity. *Annu. Rev. Neurosci.* *29*, 325–362.
- Klopfenstein, D.R., Kappeler, F., and Hauri, H.P. (1998). A novel direct interaction of endoplasmic reticulum with microtubules. *EMBO J.* *17*, 6168–6177.
- Losonczy, A., Makara, J.K., and Magee, J.C. (2008). Compartmentalized dendritic plasticity and input feature storage in neurons. *Nature* *452*, 436–441.
- Mameli, M., Balland, B., Lujan, R., and Luscher, C. (2007). Rapid synthesis and synaptic insertion of GluR2 for mGluR-LTD in the ventral tegmental area. *Science* *317*, 530–533.
- Matsuzaki, M., Honkura, N., Ellis-Davies, G.C., and Kasai, H. (2004). Structural basis of long-term potentiation in single dendritic spines. *Nature* *429*, 761–766.
- Newpher, T.M., and Ehlers, M.D. (2008). Glutamate receptor dynamics in dendritic microdomains. *Neuron* *58*, 472–497.
- Nicholson, D.A., Trana, R., Katz, Y., Kath, W.L., Spruston, N., and Geinisman, Y. (2006). Distance-dependent differences in synapse number and AMPA receptor expression in hippocampal CA1 pyramidal neurons. *Neuron* *50*, 431–442.
- Penn, A.C., Williams, S.R., and Greger, I.H. (2008). Gating motions underlie AMPA receptor secretion from the endoplasmic reticulum. *EMBO J.* *27*, 3056–3068.
- Sampo, B., Kaech, S., Kunz, S., and Banker, G. (2003). Two distinct mechanisms target membrane proteins to the axonal surface. *Neuron* *37*, 611–624.
- Santamaria, F., Wils, S., De Schutter, E., and Augustine, G.J. (2006). Anomalous diffusion in Purkinje cell dendrites caused by spines. *Neuron* *52*, 635–648.
- Schermelleh, L., Heintzmann, R., and Leonhardt, H. (2010). A guide to super-resolution fluorescence microscopy. *J. Cell Biol.* *190*, 165–175.
- Schweizer, A., Ericsson, M., Bachi, T., Griffiths, G., and Hauri, H.P. (1993). Characterization of a novel 63 kDa membrane protein. Implications for the organization of the ER-to-Golgi pathway. *J. Cell Sci.* *104*, 671–683.
- Spacek, J., and Harris, K.M. (1997). Three-dimensional organization of smooth endoplasmic reticulum in hippocampal CA1 dendrites and dendritic spines of the immature and mature rat. *J. Neurosci.* *17*, 190–203.
- Sprague, B.L., and McNally, J.G. (2005). FRAP analysis of binding: proper and fitting. *Trends Cell Biol.* *15*, 84–91.
- Spruston, N. (2008). Pyramidal neurons: dendritic structure and synaptic integration. *Nat. Rev. Neurosci.* *9*, 206–221.
- Sutton, M.A., Ito, H.T., Cressy, P., Kempf, C., Woo, J.C., and Schuman, E.M. (2006). Miniature neurotransmission stabilizes synaptic function via tonic suppression of local dendritic protein synthesis. *Cell* *125*, 785–799.
- Terasaki, M., Slater, N.T., Fein, A., Schmidek, A., and Reese, T.S. (1994). Continuous network of endoplasmic reticulum in cerebellar Purkinje neurons. *Proc. Natl. Acad. Sci. USA* *91*, 7510–7514.
- Vedrenne, C., and Hauri, H.P. (2006). Morphogenesis of the endoplasmic reticulum: beyond active membrane expansion. *Traffic* *7*, 639–646.
- Vedrenne, C., Klopfenstein, D.R., and Hauri, H.P. (2005). Phosphorylation controls CLIMP-63-mediated anchoring of the endoplasmic reticulum to microtubules. *Mol. Biol. Cell* *16*, 1928–1937.
- Ye, B., Zhang, Y., Song, W., Younger, S.H., Jan, L.Y., and Jan, Y.N. (2007). Growing dendrites and axons differ in their reliance on the secretory pathway. *Cell* *130*, 717–729.

EXTENDED EXPERIMENTAL PROCEDURES

Constructs

GFP-tagged WT-GluA1 and GluA2 constructs (GluA1WT-PRK5-GFP and GluA2WT-PC3.1-GFP) were gifts from Dr. Richard Huganir (Johns Hopkins University). HA-tagged WT-GluA2 (pGW1-GluA2WT-HA) was a gift from Dr. Morgan Sheng (Genentech). HA-tagged WT-GluA1 were generated by cloning the PCR amplified HA open reading frame (ORF) into GluA1WT-PRK5-GFP as a MluI fragment which replaced the GFP ORF. pmCherry-N1 was derived from an mCherry encoding construct (Giepmans et al., 2006) provided by Dr. Roger Tsien (University of California, San Diego). The mCherry ORF was PCR amplified and ligated as an AgeI-BsrGI insert into the pEGFP-N1 backbone (Clontech) where it replaced GFP. VSVGts045-GFP, GT-GFP (Horton and Ehlers, 2003) and β -actin-mCherry (Helton et al., 2008) have been described previously. VSVGts045-tdT and VSVGts045-mCh were produced by replacing GFP by tdTomato or mCherry in GFP-tagged VSVGts045 construct. The GFP-SERCA2a encoding plasmid (Fukatsu et al., 2004) was a gift from Dr. K. Mikoshiba (RIKEN Brain Science Institute, Japan). The VAMP2-SEP encoding plasmid was a gift from Dr. George Augustine (Korea Institute of Science and Technology).

GFP-tagged ER-GluA1 and ER-GluA2 were generated from GluA1WT-PRK5-GFP and GluA2WT-PC3.1-GFP by site-directed mutagenesis (Stratagene) of their glutamate binding site (Figure S1A) (Greger et al., 2007; Grunwald and Kaplan, 2003), which led to a retention in the ER and diminished surface expression (Figures S1B and S1C). Receptors assembled from these subunits were still able to hetero-oligomerize (Figure S1D), demonstrating that ER-retention was not due to a failure to initiate folding and assembly.

GFP tagged ER-VSVG was generated from VSVGts045-GFP constructs (Horton and Ehlers, 2003) by site-directed mutagenesis of VSVGts45 COPII binding domains (Nishimura and Balch, 1997; Sevier et al., 2000; Figure S1), which led to constitutive retention in the ER (Figures S1F and S1G). Photoactivatable ER-VSVG (ER-VSVG-paGFP) was produced by replacing GFP by paGFP (Patterson and Lippincott-Schwartz, 2002) in the GFP-tagged ER-VSVG construct. PM-pHluorin (PM-pHluo) was generated by PCR amplification of the superecliptic pHluorin (Miesenbock et al., 1998; Sankaranarayanan et al., 2000) from a plasmid provided by Dr. George Augustine (Korea Institute of Science and Technology), and cloned as a BglII-Sall insert downstream and in frame with the signal peptide sequence of the cell-surface expression type1 membrane protein backbone pDisplay (Invitrogen). The YFP-tagged GT46 encoding plasmid (Kenworthy et al., 2004; Pralle et al., 2000) was a gift from Dr. S. Grinstein (University of Toronto).

CLIMP63-WT, CLIMP63-S3A, S17A, S19A (3A), CLIMP63-S3E, S17E, S19E (3E) (Vedrenne et al., 2005) constructs were gifts from Dr. H. P. Hauri (University of Basel, Switzerland). mCherry-tagged constructs were generated by PCR amplification of the CLIMP63 ORF as a XhoI-EcoRI fragment inserted into pmCherry-N1. For expression in neurons, the CMV promoter of these plasmids was attenuated as described (Hanus et al., 2006) and all constructs were verified by sequencing. GFP-homer1C construct was a gift from Dr. Daniel Choquet (Université de Bordeaux, France).

shRNA Knockdown of CLIMP63

For shRNA knockdown of CLIMP63, we used the following target sequence: UCAACCGUAUUAGUGAAGUUCUACA. The DNA oligonucleotides containing the shRNA target sequence, a 10 nucleotide loop region (TTGATATCCG), and the shRNA antisense sequence were ligated and cloned into pLentilox3.7 (a gift from Dr. Tyler Jacks, MIT) (Kennedy et al., 2010) modified to express tdTomato as a cell fill under a synapsin I promoter. pLentilox3.7 expressing a scrambled shRNA sequence was used as a negative control. The efficacy of our shRNA sequences was assessed by immunocytochemistry and immunoblotting in hippocampal neurons transduced with pLentilox3.7 harboring either scrambled control shRNA or shRNA targeting CLIMP63, and resulted in a 65% reduction of CLIMP63 levels. For FRAP experiments, CLIMP63 shRNA and scrambled control constructs were transfected and expressed from DIV2 to DIV11. To minimize ER stress, ER-VSVG was introduced at DIV10 by a second transfection and imaged 12–24 hr post-transfection. To monitor dendritic morphogenesis at DIV11, neurons were transduced with lentivirus expressing tdTomato upon plating with subsequent transfection of shRNA-resistant CLIMP63-3A at DIV5.

Antibodies

The following antibodies were used for immunocytochemistry (ICC), immunoprecipitation (IP), or immunoblotting (IB) at the indicated concentration/dilution. Mouse anti-VSVG (Horton and Ehlers, 2003) (ICC, 1/300), rabbit anti-GFP (Clontech, IP, 1 μ g/mL), chicken anti-GFP (Chemicon, ICC, 1:1000), mouse anti-HA (Roche, IB, 1:1000), rabbit anti-Grp78/BiP (Abcam, ICC, 1:300; IB, 1:2000), rabbit anti-Sec23 (Abcam, ICC, 1:300), mouse anti-GM130 (BD Bioscience, ICC, 1:750), rabbit anti-PERK (Cell Signaling, IB, 1:1000), mouse anti- β -actin (Sigma, IB, 1:10,000), rabbit anti-RFP (Rockland, IB, 1:1000), mouse anti-MAP2 (Millipore, ICC, 1:2000), rabbit anti-GluA1 (Kennedy et al., 2010), ICC, 1:300, mouse anti-GluA2 (Chemicon, ICC, 1:300), goat rhodamine-RX or FITC-conjugated anti-IgG secondary antibodies (Jackson Laboratory, ICC, 0.75 μ g/mL), goat Alexa 647-conjugated secondary antibodies (Molecular Probes, ICC, 1:400), HRP-conjugated (Amersham, IB) and IRDye secondary antibodies (Li-Cor, IB, 1:15,000).

A custom anti-CLIMP63 rabbit polyclonal antibody was raised (Open Biosystems) against rat CLIMP63 amino acids 14–27 (peptide CHGAASP(pS)DKGAHPSG, Open Biosystems) and characterized as described in Figure S6A. Unchanged antibody recognition of wild-type CLIMP63 upon increased (2 μ M PMA, Tocris) or decreased (lambda phosphatase) phosphorylation and equivalent

recognition of CLIMP63-S19A demonstrated that this antibody was not phosphospecific and could be used as a pan-CLIMP63 antibody (data not shown).

Immunoprecipitation and Immunoblotting

Immunoprecipitation experiments were performed in 293T cells. Cells were scraped in PBS supplemented with protease (Roche) and phosphatase (Sigma) inhibitor cocktails and disrupted by sonication. Membrane fractions were collected by ultracentrifugation for 30 min at 100,000 $\times g$ (Beckman Coulter Optima) and solubilized overnight at 4°C in RIPA buffer (150 mM NaCl, 25 mM Tris, 1% sodium deoxycholate, 0.1% SDS and 1% NP40, [pH 7.6]) supplemented with protease (Roche) and phosphatase inhibitor cocktails (Sigma). Proteins of interest were coimmunoprecipitated by sequential incubation with 1 μg rabbit anti-GFP for 2 hr and protein G-coated sepharose beads (GE Healthcare) for 1 hr at 4°C.

Cultured hippocampal (Figure 7G and Figure S5) neurons were directly collected in RIPA buffer supplemented with benzonase (Sigma) and protease inhibitors (Roche) in the presence or, for subsequent λ phosphatase treatment, in the absence of phosphatase inhibitor cocktail (Sigma). For analysis of brain tissue (Figure S6A), postnatal day 7 hippocampi were dissected in Gey's balanced saline solution supplemented with 6.5% glucose and homogenized in 4 mM HEPES and 1.32 M sucrose, (pH 7.4), and then lysed for 1 hr at 4°C with 0.3% SDS in the presence of benzonase (Sigma). Lysates were resolved by SDS-PAGE in 4%–12% Bis-Tris gels (Invitrogen) and analyzed by immunoblotting using chemiluminescence (ECL Plus, GE Healthcare) or near infrared fluorescence (Li-Cor Lifesciences Inc.).

Immunocytochemistry

Cells were fixed for 15 min at RT in 4% paraformaldehyde/PBS (Serva, Germany) and then incubated for 30 min in 5% BSA/PBS (blocking solution) after 15 min permeabilization in 0.15% (w/v) Triton X-100/PBS. Incubations with primary and secondary antibodies were performed in 1.5% BSA/PBS either overnight at 4°C or for 1 hr at RT. Coverslips were mounted on glass slides in ImmuMount medium (Thermo).

Sec23 immunolabeling was performed with a separate protocol (Hammond and Glick, 2000; Horton and Ehlers, 2003). In brief, cells were first fixed in ice-cold methanol for 3 min, rehydrated in 0.1% N-octyl-beta-D-glucopyranoside incubated (OGP) and 100 μM of the cross linker bis-sulfosuccinimidyl for 30 min at RT and incubated in 0.1% ethylenediamine-HCl (pH 7.5) for 15 min and blocked in the presence of OGP in 3% fish gelatin.

For labeling of surface AMPA receptors, neurons were incubated with primary antibodies for 12 min at room temperature before fixation and were then processed as described above.

Image Acquisition and Analysis

Confocal imaging was performed using a 60 \times 1.4 NA objective on a TE300 Nikon inverted microscope equipped with a CSU10 spinning disk confocal unit (Yokugawa, Inc.), an EM-CCD camera (Hamamatsu, Inc.), and a custom 405, 488, 568, and 640 nm diode-laser illumination module (Prairie Technologies, Inc.). Photobleaching and photoactivation experiments were performed using a 63 \times 1.4 NA objective on a Zeiss LSM5-LIVE inverted confocal microscope, with the pinhole open at 5–6 Airy units and images acquired using 2 \times 2 pixel binning. For long-term imaging experiments (12–24 hr), neurons were imaged in conditioned Neurobasal/B27 medium (Invitrogen) supplemented with 7.5 mM HEPES in a 5% CO₂ atmosphere using a 20 \times 0.8 NA objective on a Zeiss LSM5-LIVE inverted confocal microscope. Live cell imaging experiments were performed at 32°C (VSVGts) or 37°C. All image analysis was performed using Metamorph software (Universal Imaging Corporation).

Variation of ER fluorescence and Sec23 levels along dendrites

Integrated fluorescence intensities were measured after application of a 3 \times 3 matrix low pass filter and background correction. To exclude ER fluorescence variation due to local heterogeneity of dendritic shapes, ER fluorescence variation coefficients throughout dendrites (standard deviation / mean) were normalized to the pixel-to-pixel fluorescence correlation index measured for GFP and a red cell fill (mCherry). Sec23 immunoreactivity was measured in segments of dendrites defined by 5 and 10 μm radius circles centered at branch points. Enrichment at branch point was quantified as the ratio of average fluorescence in the center 5 μm segment to the average fluorescence in the two 2.5 μm long flanking segments.

VSVGts accumulation in Golgi outposts at dendritic branch points

Z-stacks of GT-GFP and VSVGts-mChy were acquired at 5 min (for early time points, 10–30 min after 39–32°C temperature shift) or 10 min (for later time points, 30–40 min after temperature shift) intervals. VSVGts-mCh fluorescence was quantified at branch points displaying GOs in the first 200 μm apical dendrite of hippocampal neurons using maximal projections. Regions of interest were traced by thresholding (GOs) or manually (BPs). BP areas were defined as sections of dendrites included in 4 μm circles centered on GOs. VSVGts-mCh accumulation was measured as the integrated fluorescence intensity inside or outside outlines of GOs within BP areas after application of a 3 \times 3 matrix low pass filter and background correction.

VAMP2 exocytosis

Time-lapse sequences (101 frames) of VAMP2-SEP were acquired in single focal planes at 1 s intervals every 10 min starting 10 min after 39°C–32°C temperature shift. Exocytosis events were identified as one step increase of SEP fluorescence and were counted in the first 200 μm proximal portions of primary and secondary dendrites that were in focus. Dendritic surfaces used to calculate event

density ($N/\mu\text{m}^2$) were traced manually. Branch points were defined as described above in $5\ \mu\text{m}$ or $2.5\ \mu\text{m}$ circles centered on large or smaller branch points, respectively.

Dendritic branch formation and zones of ER complexity

The number of new dendritic branches emerging from zones of ER-complexity was quantified in the first $200\ \mu\text{m}$ of apical dendrites. Zones of ER complexity were defined by local enrichment of CLIMP63-3E-mCh over periods of at least 5 hr and were only considered if initially localized in straight dendritic segments. Only dendritic protrusions longer than $10\ \mu\text{m}$ and maintained for at least 5 hr were quantified as newly formed branches.

AMPA receptor surface expression and synaptic levels

Surface GluA1-IR was quantified in the first $150\ \mu\text{m}$ of the apical dendrite of pyramid-shaped hippocampal neurons. Dendrites were manually traced on the overlaid images of GFP-homer1C and GluA1-IR. Only segments where synapses could be assigned to the cell of interest were included in the analysis. Surface expression was quantified as the average fluorescence measured on the entire dendrite after application of a low pass filter and background correction. For analysis of synaptic receptor clusters, $0.8\ \mu\text{m}$ circles (9 pixels) were centered on excitatory postsynaptic densities marked by homer1c-GFP and on GluA1 clusters. Synaptic clusters were defined as GluA1 clusters overlapping with homer1c-GFP (overlap of 10 pixels or more).

ER entry into spines

The low fluorescence of ER membranes in dendritic spines and the relatively low spatial resolution and high sensitivity to photobleaching of FRAP experiments did not allow for quantification of ER-VSVG mobility and ER entry into spines in the same cells. These quantifications were thus done in parallel in live cells (FRAP) and after fixation. In live cells, spines were visualized by expressing a red cell fill (mCherry) and only spiny neurons displaying with clear mushroom spines were analyzed (Wang et al., 2008) (Figure 2F). Spine density was calculated by counting protrusions regardless of their morphology (stubby, mushroom-like, etc.) (Spacek and Harris, 1997) in $10\ \mu\text{m}$ dendritic segments centered on photobleached areas. In fixed cells, spines were visualized by expressing β -actin-mCherry (Figure S2L), imaged at high resolution, and counted in 50 - $100\ \mu\text{m}$ dendritic segments. The clear visualization of ER entry into spines required a saturation of ER-VSVG-GFP signal in the dendritic shaft, and was quantified manually on an all-or-none basis using a constant fluorescence scaling. Variation of ER complexity as a function of ER entry into spines was determined by calculating partial averages of these two parameters after binning the samples in groups of increasing spine density (0.1 spine/ μm increments).

FRAP Analysis

The time required for photobleaching was < 0.5 s and was negligible compared to the duration of recovery. Only cells displaying $> 70\%$ photobleaching relative to initial fluorescence in the bleached area and a global photobleaching during image acquisition $< 15\%$ were used for analysis. All data were corrected for photobleaching during image acquisition and processed using Matlab (The Math-Works Inc.). Photobleaching was performed on $4\ \mu\text{m}$ long dendritic area (Figures 1D and 1E and Figure S1K) or otherwise specified in the Results. Experiments in neuronal dendrites were performed in dendritic segments of matched diameters at similar distances from the cell body.

FRAP in fibroblasts

The normalized fluorescence intensity $F(t)$ in bleached areas at time t was analyzed using the two-dimensional diffusion model as described (Feder et al., 1996) and fitted with the equation:

$$F(t) = \frac{F_1 + (R(F_0 - F_1) + F_1) \left(\frac{t}{t_{1/2}}\right)^\alpha}{1 + \left(\frac{t}{t_{1/2}}\right)^\alpha} \quad (1)$$

where F_0 is the fluorescence intensity before bleaching, F_1 is the fluorescence intensity immediately after bleaching, R is the recovered fluorescence fraction, and $t_{1/2}$ is the recovery halftime.

FRAP in neuronal dendrites

A custom fitting model was used for analysis according to Fick's second diffusion law (Crank, 1975). Assuming three-dimensional diffusion in cylindrical structures, the concentration C of fluorophore at position \mathbf{r} within the photobleached segment at time t , $C(\mathbf{r}, t)$, along with the concentration gradient ∇ induced by photobleaching are related by Fick's second diffusion law written as:

$$\frac{\partial C(\mathbf{r}, t)}{\partial t} = D(t) \nabla^2 C(\mathbf{r}, t) \quad (2)$$

The diffusion was considered to be potentially anomalous, implying a diffusion coefficient D varying with the transport coefficient Γ such that

$$D(t) = \frac{1}{4} \Gamma t^{\alpha-1} = D_1 t^{\alpha-1} \quad (3)$$

with r included in the photobleached rectangular profile of length $2w$, a symmetric recovery at each side of the bleached cylinder, and an absence of diffusion in the direction n perpendicular to its axis. The boundary conditions were:

$$\begin{aligned} C(w, t) &= C(-w, t) = C_0, t \geq 0, \\ C(r, t) &= 0, t = 0, \\ \left. \frac{\partial C(r, t)}{\partial n} \right|_{\Omega} &= 0 \end{aligned} \quad (4)$$

Dendrites were considered to be cylinders along which $C(r, t)$ is equal in the plane orthogonal to the cylinder axis at position r . The Equation (2) can then be approximated using a one-dimensional diffusion relationship where the second Fick's law becomes

$$\frac{\partial C(x, t)}{\partial t} = D(t) \frac{\partial^2 C(x, t)}{\partial x^2}, \quad (5)$$

with x being the distance along dendrites from the center of the photobleached rectangle. With the symmetry present at $x = 0$, boundary conditions can be written in the form:

$$\begin{aligned} C(w, t) &= C(-w, t) = C_0, t \geq 0, \\ \left. \frac{\partial C(x, t)}{\partial x} \right|_{x=0} &= 0, x = 0, t \geq 0 \\ C(x, t) &= 0, t = 0, |x| < w \end{aligned} \quad (6)$$

The differential Equation (6) was solved using the method of separation of variables and integration by parts, resulting in an equation of the form:

$$C(x, t) = C_0 - \frac{4C_0}{\pi} \sum_{n=0}^{+\infty} \frac{(-1)^n}{2n+1} \exp\left(-\frac{D_1(2n+1)^2 \pi^2 t^\alpha}{4\alpha w^2}\right) \cos\left(\frac{(2n+1)\pi x}{2w}\right) \quad (7)$$

The normalized fluorescence intensity $F(t)$ observed at time ≥ 0 and calculated in the entire bleached rectangle could thus be expressed in the form:

$$F(t) = R \left(1 - \frac{8}{\pi^2} \sum_{n=0}^{+\infty} \frac{1}{(2n+1)^2} \exp\left(-\frac{D_1(2n+1)^2 \pi^2 t^\alpha}{4\alpha w^2}\right) \right) \quad (8)$$

with R the recovered fraction, D_1 the apparent diffusion coefficient, and α an "anomalous" coefficient, which were calculated by minimization of the mean-squared error. The sum used for the integration was truncated with n varying from 0 to a nonnegative integer N (chosen as 10 across the analysis). Throughout the present study, calculated α coefficients were not significantly affected under any of our experimental conditions (see also Table S1).

The quality of FRAP plot fitting was estimated by R-square values (Bevington, 1992). Only plots showing fitting within 90% statistical confidence were included in our analysis (>90% of the neurons we monitored).

Modeling Nascent AMPA Receptor Diffusion in the Dendritic ER Synthesis rates and accumulation of nascent GluA1 and GluA2

Since ER-bound ribosomes (Figure 4A) and Golgi outposts (Horton et al., 2005) concentrate at branch points, we selected branch points as points of origin of newly synthesized AMPA receptors. However, the model can be applied to any arbitrary point source or multiple point sources along the dendrite. Due to the combined effect of translation initiation, elongation, protein folding, and subunit assembly, it is difficult to estimate realistic synthesis rates of a given membrane protein a priori (Hershey, 1991). Rough estimates of nascent GluA1 and GluA2 accumulation rates were extrapolated from protein elongation rates measured in vitro (~6 amino acids/second per active ribosome) (Hershey, 1991), the estimated number of ER-bound ribosomes present at dendritic branch points in our EM micrographs, the relative abundance of GluA1 and GluA2 mRNA in hippocampal neuron dendrites reported in the literature (Grooms et al., 2006; Poon et al., 2006; Tsuzuki et al., 2001), and the relative abundance of secreted and transmembrane proteins found in the murine transcriptome (<http://locate.imb.uq.edu.au/>; Sprenger et al., 2008). Single cell PCR measurement indicate that GluA1 and GluA2 mRNAs represent approximately 1/240 and 1/500 of total cellular mRNAs in cultured hippocampal pyramidal neurons, respectively (Tsuzuki et al., 2001). Assuming that GluA2 mRNA displays the same relative dendritic enrichment as GluA1 mRNA (~3.2) (Grooms et al., 2006; Poon et al., 2006), GluA1 and GluA2 encoding mRNAs can be expected to represent ~1/75 and ~1/150 of total dendritic mRNAs, respectively. Among the 58,128 protein sequences present in the RIKEN FANTOM mouse

protein sequence database (Carninci et al., 2005), 4231 correspond to secreted (signal-peptide containing) proteins, and 14,088 correspond to membrane (transmembrane domain containing) proteins (<http://locate.imb.uq.edu.au/>; Sprenger et al., 2008). Although this estimation does not take into account mitochondrial transmembrane proteins, cytoplasmic proteins processed by ER-bound ribosomes, or neuron-specific transcriptomes, one can estimate that ~31.5% of mRNAs will be processed by ER-bound ribosomes in a generic murine cell. Assuming that mRNA dendritic enrichment preserves these proportions, one can estimate that GluA1 and GluA2 mRNAs represent ~1/23.6 and ~1/47.2 of dendritic mRNAs processed by ER-bound ribosomes, respectively. Finally, assuming optimal and equal translation initiation rates and an average size of 700 codons for all dendritic mRNAs, the ~100 ER-bound ribosomes found at a single generic dendritic branch point could in principle assemble 600 amino acids per second, thus 51 proteins and therefore ~2.2 GluA1 and ~1.1 GluA2 per minute. The potential effects of their association with ER chaperone proteins, posttranslational modifications, and ER associated degradation (ERAD) on nascent receptor diffusion were not considered in the present model.

Computation of nascent receptor densities along dendrites

Reference dendritic trees were obtained by imaging DIV24 hippocampal neurons expressing a red cell fill. Dendritic trees were segmented into 7 μm long segments (the sized of bleached area used for FRAP) starting at dendritic branch points. Apparent diffusion coefficients estimated for branch points or straight spiny dendrites (see also Table S2) were assigned to the resulting structures. The density of nascent GluA1 and GluA2 produced at the rates described above at a randomly chosen dendritic branch point over time was then computed in Matlab using a modified version of Equation (7), allowing the incorporation of distinct apparent diffusion coefficients assigned to specific dendritic regions. Shown in Figure S3 and Movie S2 are color-coded densities of nascent GluA1 computed at different time points.

For the analysis, Equation (5) was modified so that D became a function of the distance x along the dendritic tree from the origin. With x_s and R_s being the coordinate of the origin branch point and associated protein synthesis rate, respectively, the diffusion within a dendritic branch i , was expressed in the form:

$$\frac{\partial C_i(x_i, t)}{\partial t} = \begin{cases} D(x_i) \frac{\partial^2 C_i(x_i, t)}{\partial x_i^2} + R_s, & \text{if } x_i = x_s, \\ D(x_i) \frac{\partial^2 C_i(x_i, t)}{\partial x_i^2}, & \text{otherwise.} \end{cases} \quad (9)$$

Assuming that dendritic branches are narrow enough to be considered as elastic tubes along which diffusion rate and protein density is constant at any arbitrarily small cross section, protein entry into dendritic branch points upon bifurcation will be directly proportional to the cross sectional area of each branch. For example, considering protein flow entering branches 1 and 2 from branch 0, with $F_i(x_b)$ $i = 0, 1, 2$ the transfer rate per area unit, D_i the diffusion coefficient at the branch point x_b , and r_i the radius of branch i , mass conservation at branch points implies that:

$$\pi r_0^2 F_0 = \pi r_1^2 F_1 + \pi r_2^2 F_2 \Rightarrow r_0^2 D_0 \frac{\partial C_0(x_b, t)}{\partial t} = r_1^2 D_1 \frac{\partial C_1(x_b, t)}{\partial t} + r_2^2 D_2 \frac{\partial C_2(x_b, t)}{\partial t}. \quad (10)$$

With T and B the two sets encompassing all dendritic ends and branch points, respectively, nascent protein diffusion throughout the entire dendritic tree can be described using the following partial differential equations:

$$\frac{\partial C_i(x_i, t)}{\partial t} = \begin{cases} D(x_i) \frac{\partial^2 C_i(x_i, t)}{\partial x_i^2} + R_s, & \text{if } x_i = x_s, \\ D(x_i) \frac{\partial^2 C_i(x_i, t)}{\partial x_i^2}, & \text{otherwise.} \end{cases} \quad (11)$$

$$r_0^2 D_0 \frac{\partial C_0(x_b, t)}{\partial t} = r_1^2 D_1 \frac{\partial C_1(x_b, t)}{\partial t} + r_2^2 D_2 \frac{\partial C_2(x_b, t)}{\partial t}, \quad \forall x_b \in B$$

$$\frac{\partial C_i(x_e, t)}{\partial x_e} = 0, \quad \forall x_e \in T$$

$$C_i(x_i, 0) = 0, \quad \forall x_i.$$

Unlike FRAP data analysis where closed form solutions could be derived, it was difficult to obtain analytical solution of (11). We thus used a finite difference method to solve (11). At time t , we could approximate:

$$\frac{\partial^2 C_i(x_i, t)}{\partial x_i^2} \approx \frac{C_i(x_i - \Delta x, t) - 2C_i(x_i, t) + C_i(x_i + \Delta x, t)}{\Delta x^2}, \quad (12)$$

where $\Delta x > 0$ is a small step size. We then updated $C_i(x_i, t + \Delta t)$ using the relations:

$$\begin{aligned}
C_i(x_i, t + \Delta t) &\approx C_i(x_i, t) + \frac{\partial^2 C_i(x_i, t)}{\partial x_i^2} \Delta t \\
&\approx C_i(x_i, t) + \frac{C_i(x_i - \Delta x, t) - 2C_i(x_i, t) + C_i(x_i + \Delta x, t)}{\Delta x^2} \Delta t, \quad \text{if } x_i \neq x_s,
\end{aligned} \tag{13}$$

where Δt is a small time step size. When $x_i = x_s$, we only needed to add $R_s \Delta t$ to the right hand side of (13). At the branch point x_b , we thus have

$$r_0^2 D_0 \frac{C_0(x_b, t + \Delta t) - C_0(x_b - \Delta x, t + \Delta t)}{\Delta x} = r_1^2 D_1 \frac{C_1(x_b + \Delta x, t + \Delta t) - C_1(x_b, t + \Delta t)}{\Delta x} + r_2^2 D_2 \frac{C_2(x_b + \Delta x, t + \Delta t) - C_2(x_b, t + \Delta t)}{\Delta x} \tag{14}$$

Note that $C_0(x_b, t + \Delta t) = C_1(x_b, t + \Delta t) = C_2(x_b, t + \Delta t)$. Therefore,

$$C_0(x_b, t + \Delta t) = \frac{r_0^2 D_0 C_0(x_b - \Delta x, t + \Delta t) + r_1^2 D_1 C_1(x_b + \Delta x, t + \Delta t) + r_2^2 D_2 C_2(x_b + \Delta x, t + \Delta t)}{r_0^2 D_0 + r_1^2 D_1 + r_2^2 D_2} \tag{15}$$

Finally, the third boundary condition in (11) implies that: $C_i(x_e, t + \Delta t) = C_i(x_e - \Delta x, t + \Delta t)$, $\forall x_e \in T$.

By executing (13)-(15) in Matlab, we obtained the numerical solution of (11).

Electrophysiology

Whole-cell voltage clamp recordings were performed in DIV10-13 neurons after expressing mCherry and CLIMP63 phosphomutants for 3-6 days. Neurons were held at -60 mV using a MultiClamp 700A amplifier (Axon Instruments, CA) controlled by a Pentium PC running MultiClamp Commander and pClamp (Axon Instruments) in extracellular solution containing (in mM) 150 NaCl, 5 KCl, 10 HEPES, 1 MgCl₂, 30 D-glucose, 2 CaCl₂, 0.001 TTX and 0.03 bicuculline (330 mOsm/l, pH 7.4). Recording pipettes, with resistances between 3-5 M Ω , were filled with a solution containing (in mM) 30 CsSO₄, 70 K₂SO₄, 25 HEPES, 25 N-methyl-D-glucamine, 0.1 CaCl₂, 1 EGTA, 2 Na₂ATP and 0.1 leupeptin (300 mOsm/l, pH 7.2). Data were analyzed using MiniAnalysis software (Synaptosoft, Decatur, GA). mEPSC traces with amplitude greater than 5 pA and rise times (from the onset to the peak) less than 5 ms were included in the analysis.

Statistics

Throughout the paper, data are presented as means \pm SEM. The number of cells and independent experiments used for quantifications are indicated in the text or in the figure legends. Statistical significance was determined using 2-tailed unpaired or paired t tests when comparing paired sets of data obtained in cell populations or in individual cells, respectively. ANOVA was used when simultaneously comparing more than two data sets.

SUPPLEMENTAL REFERENCES

- Bevington, P.R., and Robinson, D.K. (1992). *Data Reduction and Error Analysis for the Physical Sciences*, Second Edition (London, McGraw-Hill).
- Carninci, P., Kasukawa, T., Katayama, S., Gough, J., Frith, M.C., Maeda, N., Oyama, R., Ravasi, T., Lenhard, B., Wells, C., et al. (2005). The transcriptional landscape of the mammalian genome. *Science* *309*, 1559-1563.
- Crank, J. (1975). *The Mathematics of Diffusion*, Second Edition (Clarendon Press Oxford).
- Feder, T.J., Brust-Mascher, I., Slattery, J.P., Baird, B., and Webb, W.W. (1996). Constrained diffusion or immobile fraction on cell surfaces: a new interpretation. *Biophys. J.* *70*, 2767-2773.
- Fukatsu, K., Bannai, H., Zhang, S., Nakamura, H., Inoue, T., and Mikoshiba, K. (2004). Lateral diffusion of inositol 1,4,5-trisphosphate receptor type 1 is regulated by actin filaments and 4.1N in neuronal dendrites. *J. Biol. Chem.* *279*, 48976-48982.
- Giepmans, B.N., Adams, S.R., Ellisman, M.H., and Tsien, R.Y. (2006). The fluorescent toolbox for assessing protein location and function. *Science* *312*, 217-224.
- Greger, I.H., Ziff, E.B., and Penn, A.C. (2007). Molecular determinants of AMPA receptor subunit assembly. *Trends Neurosci.* *30*, 407-416.
- Grooms, S.Y., Noh, K.M., Regis, R., Bassell, G.J., Bryan, M.K., Carroll, R.C., and Zukin, R.S. (2006). Activity bidirectionally regulates AMPA receptor mRNA abundance in dendrites of hippocampal neurons. *J. Neurosci.* *26*, 8339-8351.
- Grunwald, M.E., and Kaplan, J.M. (2003). Mutations in the ligand-binding and pore domains control exit of glutamate receptors from the endoplasmic reticulum in *C. elegans*. *Neuropharmacology* *45*, 768-776.
- Hammond, A.T., and Gluck, B.S. (2000). Dynamics of transitional endoplasmic reticulum sites in vertebrate cells. *Mol. Biol. Cell* *11*, 3013-3030.
- Hanus, C., Ehrensperger, M.V., and Triller, A. (2006). Activity-dependent movements of postsynaptic scaffolds at inhibitory synapses. *J. Neurosci.* *26*, 4586-4595.
- Helton, T.D., Otsuka, T., Lee, M.C., Mu, Y., and Ehlers, M.D. (2008). Pruning and loss of excitatory synapses by the parkin ubiquitin ligase. *Proc. Natl. Acad. Sci. USA* *105*, 19492-19497.
- Hershey, J.W. (1991). Translational control in mammalian cells. *Annu. Rev. Biochem.* *60*, 717-755.

- Horton, A.C., and Ehlers, M.D. (2003). Dual modes of endoplasmic reticulum-to-Golgi transport in dendrites revealed by live-cell imaging. *J. Neurosci.* *23*, 6188–6199.
- Horton, A.C., Racz, B., Monson, E.E., Lin, A.L., Weinberg, R.J., and Ehlers, M.D. (2005). Polarized secretory trafficking directs cargo for asymmetric dendrite growth and morphogenesis. *Neuron* *48*, 757–771.
- Kennedy, M.J., Davison, I.G., Robinson, C.G., and Ehlers, M.D. (2010). Syntaxin-4 defines a domain for activity-dependent exocytosis in dendritic spines. *Cell* *141*, 524–535.
- Kenworthy, A.K., Nichols, B.J., Remmert, C.L., Hendrix, G.M., Kumar, M., Zimmerberg, J., and Lippincott-Schwartz, J. (2004). Dynamics of putative raft-associated proteins at the cell surface. *J. Cell Biol.* *165*, 735–746.
- Miesenbock, G., De Angelis, D.A., and Rothman, J.E. (1998). Visualizing secretion and synaptic transmission with pH-sensitive green fluorescent proteins. *Nature* *394*, 192–195.
- Nishimura, N., and Balch, W.E. (1997). A di-acidic signal required for selective export from the endoplasmic reticulum. *Science* *277*, 556–558.
- Patterson, G.H., and Lippincott-Schwartz, J. (2002). A photoactivatable GFP for selective photolabeling of proteins and cells. *Science* *297*, 1873–1877.
- Poon, M.M., Choi, S.H., Jamieson, C.A., Geschwind, D.H., and Martin, K.C. (2006). Identification of process-localized mRNAs from cultured rodent hippocampal neurons. *J. Neurosci.* *26*, 13390–13399.
- Pralle, A., Keller, P., Florin, E.L., Simons, K., and Horber, J.K. (2000). Sphingolipid-cholesterol rafts diffuse as small entities in the plasma membrane of mammalian cells. *J. Cell Biol.* *148*, 997–1008.
- Sankaranarayanan, S., De Angelis, D., Rothman, J.E., and Ryan, T.A. (2000). The use of pHluorins for optical measurements of presynaptic activity. *Biophys. J.* *79*, 2199–2208.
- Sevier, C.S., Weisz, O.A., Davis, M., and Machamer, C.E. (2000). Efficient export of the vesicular stomatitis virus G protein from the endoplasmic reticulum requires a signal in the cytoplasmic tail that includes both tyrosine-based and di-acidic motifs. *Mol. Biol. Cell* *11*, 13–22.
- Spacek, J., and Harris, K.M. (1997). Three-dimensional organization of smooth endoplasmic reticulum in hippocampal CA1 dendrites and dendritic spines of the immature and mature rat. *J. Neurosci.* *17*, 190–203.
- Sprenger, J., Lynn Fink, J., Karunaratne, S., Hanson, K., Hamilton, N.A., and Teasdale, R.D. (2008). LOCATE: a mammalian protein subcellular localization database. *Nucleic Acids Res.* *36*, D230–D233.
- Tsuzuki, K., Lambolez, B., Rossier, J., and Ozawa, S. (2001). Absolute quantification of AMPA receptor subunit mRNAs in single hippocampal neurons. *J. Neurochem.* *77*, 1650–1659.
- Vedrenne, C., Klopfenstein, D.R., and Hauri, H.P. (2005). Phosphorylation controls CLIMP-63-mediated anchoring of the endoplasmic reticulum to microtubules. *Mol. Biol. Cell* *16*, 1928–1937.
- Wang, Z., Edwards, J.G., Riley, N., Provance, D.W., Jr., Karcher, R., Li, X.D., Davison, I.G., Ikebe, M., Mercer, J.A., Kauer, J.A., et al. (2008). Myosin Vb mobilizes recycling endosomes and AMPA receptors for postsynaptic plasticity. *Cell* *135*, 535–548.

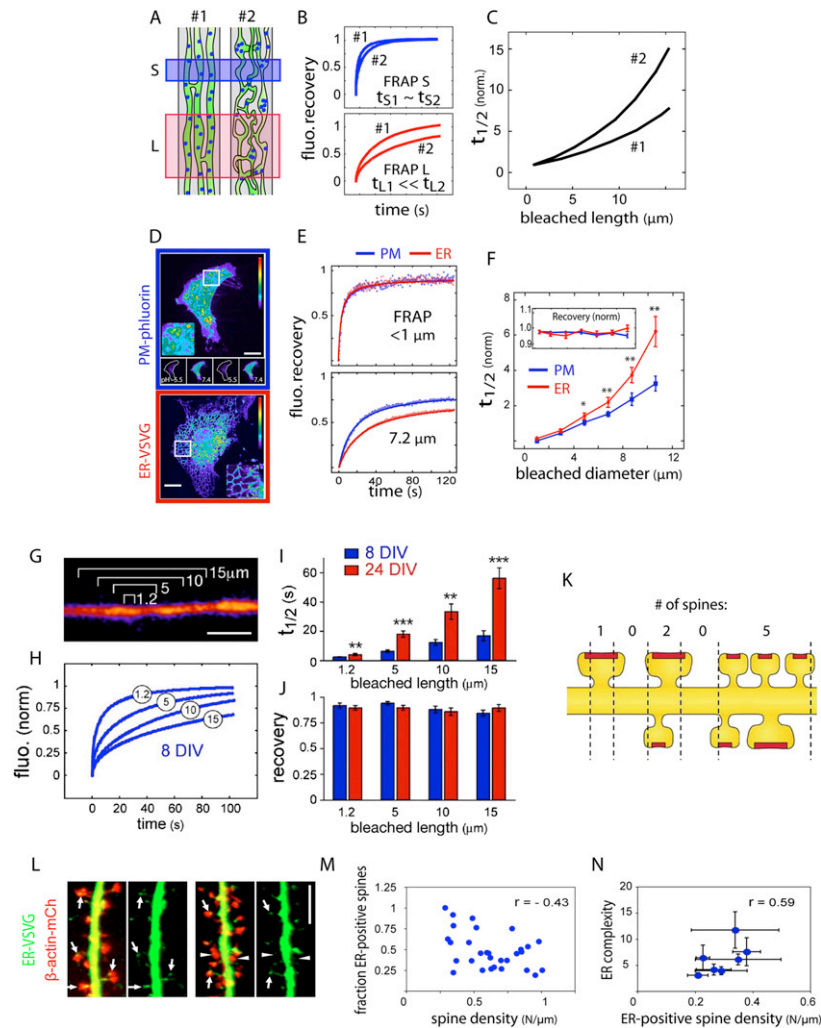


Figure S2. FRAP-Based Method to Measure ER Complexity and the Increase in ER Complexity Accompanying Dendritic Development but Unrelated to ER Entry into Dendritic Spines, Related to Figure 2

(A) Hypothetical endoplasmic reticulum (ER, green) in two dendrites with either simple (#1) or convoluted (#2) spatial organization. Blue circles indicate diffusing molecules within the ER membrane.

(B) Fluorescence recovery in small (S, blue) and large (L, red) dendritic segments from #1 and #2. Dendritic regions with more complex fluorophore-accessible volumes will display a more pronounced slowing of recovery as the size of the bleached area increases.

(C) Increased complexity is revealed by plotting normalized recovery rates as a function of the size of the bleached areas. Hence, by comparing the ratio of fluorescence recovery rates derived from large areas (typically $> 5 \mu\text{m}$) to small areas (typically $1 \mu\text{m}$), one obtains an index of the apparent complexity of the fluorophore-accessible volume.

(D) Fluorescence of the plasma membrane marker PM-pHluorin (top) and the ER marker ER-VSVG-YFP (bottom) in HeLa cells (pseudocolor scale). Top inset shows sequential switches to pH5.5 and quenching of the surface PM-pHluorin. Bottom inset shows reticular structure of the ER. The scale bar represents $10 \mu\text{m}$.

(E) Raw (circles) and fitted (lines) recovery plots after photobleaching PM-pHluorin (blue) or ER-VSVG (red) in $1 \mu\text{m}$ (top) or $7.2 \mu\text{m}$ (bottom) regions. The slower recovery of ER-VSVG after bleaching a large region (bottom) indicates the more complex fluorophore-accessible volume of the ER relative to the PM.

(F) Recovery half-times ($t_{1/2}$) and recovery fractions (inset) as a function of the diameter of bleached areas for PM-pHluorin (blue) and ER-VSVG (red) normalized to values obtained with $1 \mu\text{m}$ bleached areas. Mean \pm SEM, $n = 12$ -13 measurements for each data point over two to three experiments; * $p < 0.05$, ** $p < 0.01$; t test.

(G-J) Developmental increase of ER complexity. (G) ER-VSVG distribution and position of the bleached dendritic segments (1.2 - $15 \mu\text{m}$) used for FRAP on a DIV8 hippocampal neuron. The scale bar represents $5 \mu\text{m}$. (H) Progressive slowing of ER-VSVG recovery in bleached dendrite segments of increasing length (value in white circles).

(I-J) Recovery half-times (I) and recovered fractions (J) in 1.2 , 5 , 10 and $15 \mu\text{m}$ long dendrite segments. Mean \pm SEM, $n = 20$, 21 cells in four experiments at DIV8 and DIV24, respectively; ** $p < 0.01$, *** $p < 0.001$; t test.

(K) For morphological analysis of electron micrographs, spans of serial sections defining aspiny or spiny segments of dendrites began with the first section where the base of a spine started to emerge from the dendritic shaft and ended with the section where the base of the last spine was no longer detectable.

(L) Visualization of dendritic spines (β -actin-mCh) and ER (ER-VSVG) in hippocampal neuron dendrites. Arrows and arrowheads indicate spines containing and lacking ER, respectively. The scale bar represents $5 \mu\text{m}$.

(M) Spine density does not correlate with the fraction of ER-positive spines.

(N) Lack of relationship between ER complexity and ER intrusion into spines.

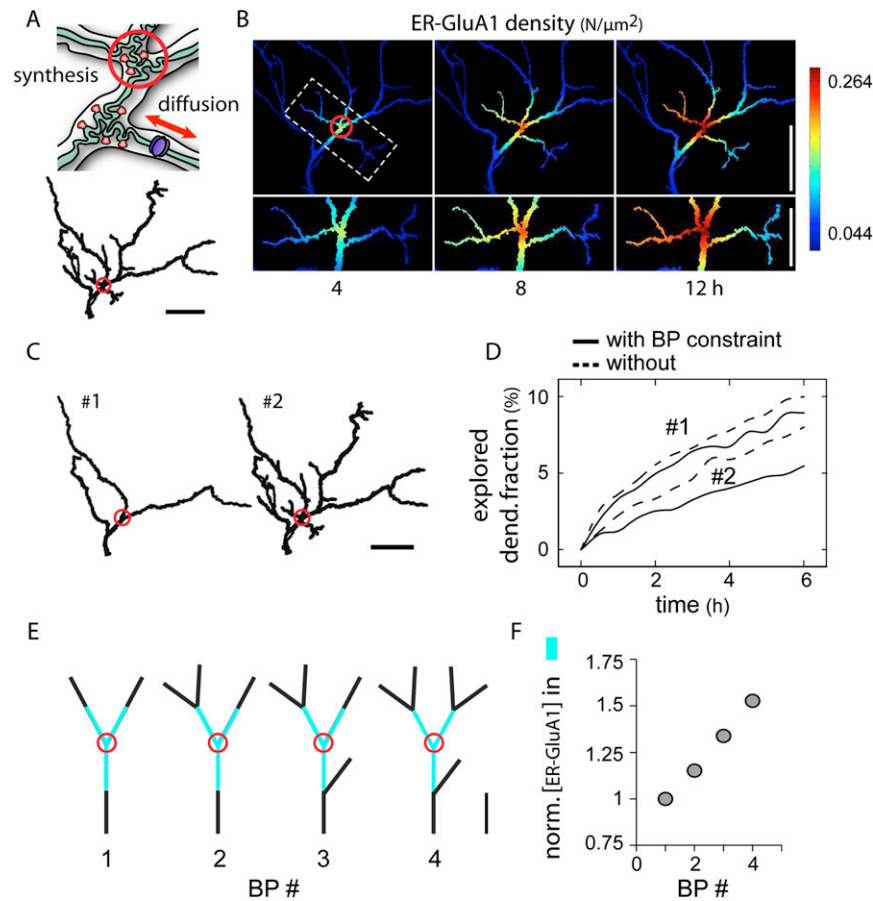


Figure S3. Compartmentalization of Nascent AMPA Receptors in the Dendritic ER, Related to Figure 3

(A) The spread of nascent AMPA receptors (blue) within the dendritic ER was simulated in actual dendritic tree templates assuming a constant rate of protein synthesis by ER-bound ribosomes (orange) at a dendritic branch point (red circle). See [Experimental Procedures](#) for details. The scale bar represents 50 μm .

(B) ER-GluA1 density at different time points after the initiation of synthesis at the branch point marked by a red circle. The area within the white dashed box is magnified in the lower panels. See [Experimental Procedures](#) for details. The scale bars represent 50 μm (upper panel) and 25 μm (lower panel).

(C) Dendritic templates with low (#1) or high (#2) degrees of branching. The scale bar represents 50 μm .

(D) Fractional exploration of the total dendritic domain over time assuming constrained diffusion at branch points (BP, plain lines) or homogenous diffusion without branch point constraint (dashed lines) in the two templates (#1, #2) shown in (C). The range of AMPA receptor exploration is reduced with increasing dendritic complexity and with constrained diffusion at branch points.

(E) Simplified dendritic templates with 0 to 3 dendritic branch points distributed at equal distances from the branch point marked as the point of synthesis (red circle). The scale bar represents 25 μm .

(F) Normalized ER-GluA1 concentrations in the dendritic subcompartment shown in blue in (E) after a 30 min synthesis period, as a function of branch point number. Branch points cumulatively increase receptor accumulation by diffusional confinement.

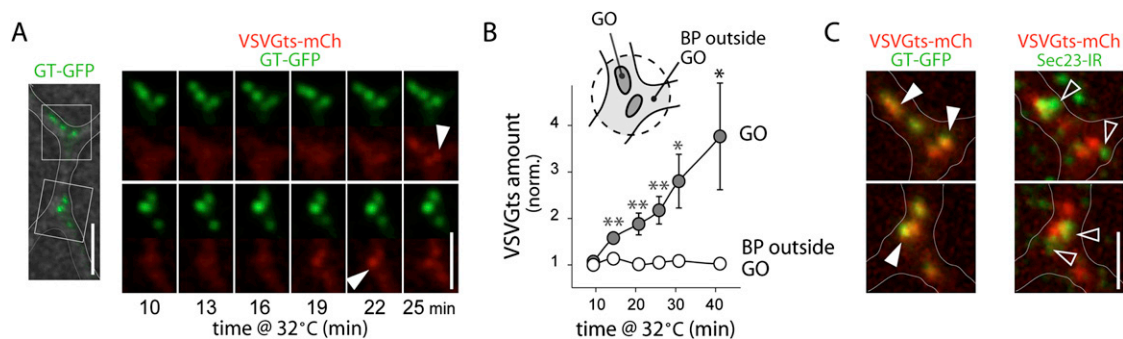


Figure S4. ER-to-Golgi Trafficking of VSVGts at Dendritic Branch Points, Related to Figure 4

(A–B) ER-released VSVGts accumulates in dendritic Golgi outposts (GOs) visualized by GFP tagged with the Golgi targeting sequence of galactosyltransferase (GT-GFP). (A) Images and time-lapse. Arrowheads indicate VSVGts-mCh accumulated in a GO. (B) Quantification of VSVGts-mCh accumulation over time. Plotted is VSVGts fluorescence colocalized with GT-GFP in Golgi outposts (GO) over time, and total VSVGts fluorescence at branch points outside GO regions labeled with GT-GFP (BP outside GO). The scale bar represents 5 μm . Mean \pm SEM, $n = 13$ cells; * $p < 0.05$, ** $p < 0.01$; ANOVA.

(C) Immunolabeling for Sec23 after accumulation of VSVGts-mCh in GOs (same dendrite as in A). Note the complete colocalization of VSVGts with GOs (white arrowheads) and the lack of colocalization with ER exit sites labeled for Sec23 (black arrowheads). The scale bar represents 2.5 μm .

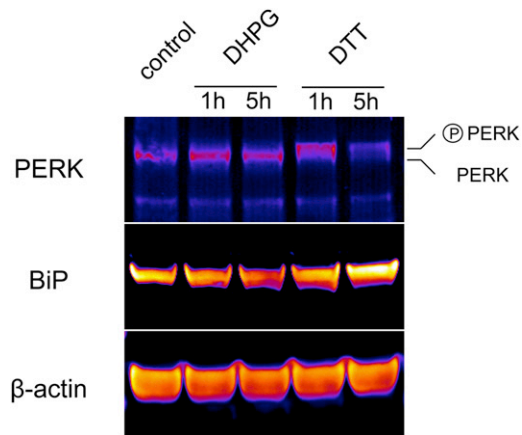


Figure S5. Absence of Detectable ER Stress upon Type I mGluR Activation by DHPG, related to Figure 5

Phospho-PERK, Grp78/BiP, and β -actin levels (immunoblotting, pseudocolored fluorescence intensities) in DIV14 hippocampal neurons in the absence or presence of DHPG or 5 mM DTT for 1 to 5 hr. In the upper blot, note the shift of PERK immunoreactivity toward higher apparent molecular mass species allowing the detection of nonphosphorylated (lower band) and phosphorylated PERK (upper band) in the presence of DTT but not DHPG. In the middle blot, note the unchanged and increased BiP expression in cells exposed to DHPG and DTT, respectively.

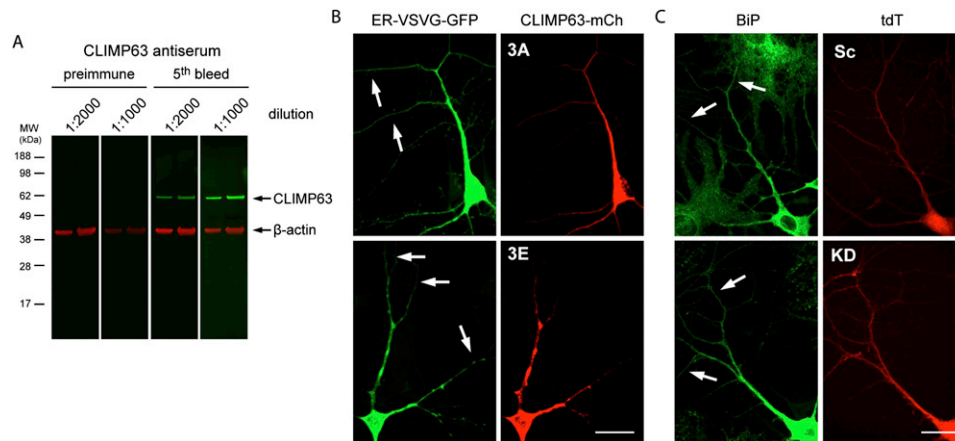


Figure S6. CLIMP63 Expression in Rat Hippocampus and Presence of ER in Distal Dendrites of Neurons Expressing CLIMP63 Mutants, Related to Figure 6

(A and B) Characterization of custom anti-CLIMP63 rabbit antibody. (A) CLIMP63 (green) and β -actin (red) immunoreactivity in postnatal day 7 (PND7) hippocampus detected by immunoblot using either preimmune or anti-CLIMP63 sera documenting the detection of a single band corresponding to CLIMP63. 10 or 20 μ g total protein was loaded in each lane.

(B) Distribution of the ER (ER-VSVG, green) in DIV14 hippocampal neurons expressing mCherry-tagged CLIMP63-3A (3A) or 3E (3E) mutants documenting the presence of the ER in distal dendrites (arrows). The scale bar represents 30 μ m.

(C) Endogenous BiP immunoreactivity (green) in DIV14 hippocampal neurons documenting the presence of the ER in distal dendrites (arrows). Neurons were transduced with scrambled (Sc) or CLIMP63 (KD) shRNA with tdTomato (tdT) reporter. The scale bar represents 30 μ m.

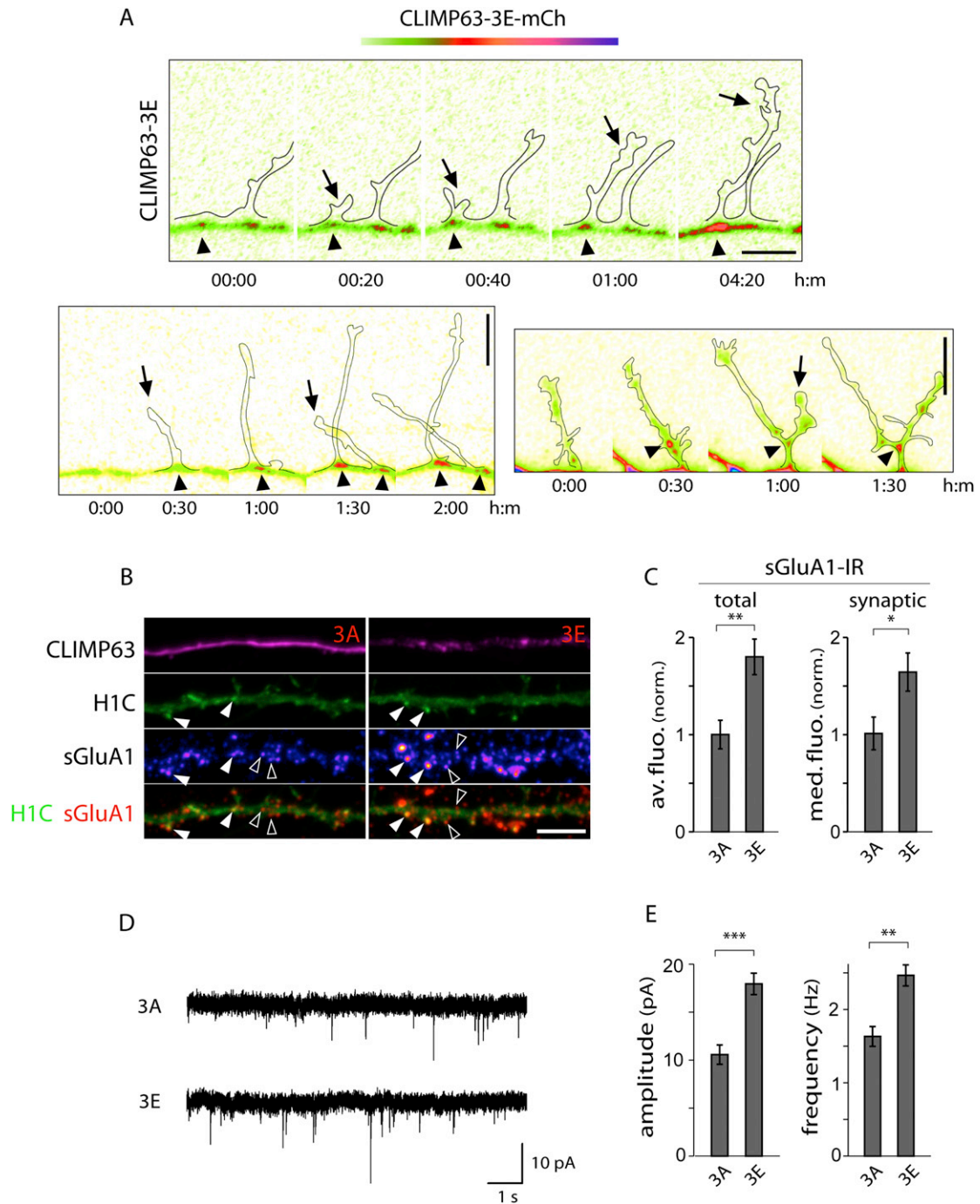


Figure S7. Concentration of CLIMP63-3E at the Base of Emerging Dendritic Branches and CLIMP63-3E Effects on AMPA Receptor Surface Expression at Synapses, Related to Figure 7

(A) CLIMP63-3E (pseudocolored) concentration at branch point (arrowheads) occurs upon new branch emergence (arrows). Outlines represent GFP expression in the emerging branch. Time in hr:min. The scale bar represents 10 μ m.

(B and C) Representative images (B) and quantification (C) of surface GluA1 (sGluA1) immunoreactivity (IR) in DIV12 hippocampal neurons expressing the postsynaptic excitatory synapse marker homer1c-GFP (H1C) with either CLIMP63-3A or CLIMP63-3E mutants. Shown in (C) are total average (av. fluo.) sGluA1-IR in dendrites or median (med. fluo.) synaptic IR (arrowheads in B) after normalization to CLIMP63-3A values. Empty arrowheads in (B) mark extrasynaptic clusters of sGluA1. The scale bar represents 5 μ m. Mean \pm SEM, $n = 13$ –14 cells, two experiments; * $p < 0.05$, ** $p < 0.01$, t test.

(D and E) Electrophysiological recordings (D) and quantification (E) of mEPSCs recorded at the soma from DIV11-DIV13 hippocampal neurons expressing CLIMP63-3A (3A) or CLIMP63-3E (3E). Note the increased mEPSC amplitude and frequency in neurons expressing CLIMP63-3E. Mean \pm SEM, $n = 12$ –13 cells, three to four experiments for each; * $p < 0.05$, ** $p < 0.01$, *** $p < 0.001$; t test.